

**UNIVERSITA' DEGLI STUDI DI MILANO-BICOCCA**  
Facoltà di Scienze Matematiche, Fisiche e Naturali  
Dipartimento di Fisica

**“Ultrashort High Intensity Laser Matter Interaction Studies”**



**Tesi di Dottorato in Fisica e Astronomia XXI Ciclo**

Renato Redaelli

Direttore di Tesi: Prof. Dimitri Batani

Coordinatore: Prof. Claudio Destri

Anno Accademico 2008-2009

<b>Introduction</b>	pag. 1
<b>PART 1 : EOS of CARBON</b>	
Introduction	pag. 4
<b>Chapter 1: Laser-plasma interactions</b>	pag. 6
1.1.1 Plasma generation	pag. 6
1.1.2 Different plasma regions	pag. 6
1.1.3 Laser absorption	pag. 7
1.1.4 Energy transfer	pag. 8
1.1.5 Hydrodynamics	pag. 9
1.2.1 "Inertial Confinement Fusion": ICF	pag. 11
1.2.2 "Equations Of State": EOS	pag. 14
Thomas-Fermi model	pag. 15
Shock waves	pag. 16
Impedence mismatch method	pag. 19
1.2.3 Astrophysics	pag. 23
1.3 Experimental problems	pag. 25
1.3.1 Laser disuniformities	pag. 25
1.3.2 Optical omogeneization techniques	pag. 25
Random phase plate	pag. 26
Phase zone plate	pag. 26
Streak cameras operating principle	pag. 29
Bibliography Part 1- Chapter one	pag. 31
<b>Chapter 2 : EOS of Carbon</b>	pag. 34
Introduction	pag. 34
2.1.1 Grumbach - Martin phase diagram	pag. 36
2.1.2 PALS laser and experimental set up	pag. 37
2.1.3 Carbon targets	pag. 39
Supersonic Cluster Beam deposition	pag. 39
General Atomic carbon targets	pag. 42
2.1.4 Results	pag. 42
2.1.5 Conclusion	pag. 46
Bibliography Part 1- Chapter 2	pag. 47
Appendix 1	pag. 49
<b>PART 2 : Polarimetric detection of laser induced ultrashort magnetic pulses in overdense plasma</b>	pag. 60

## **Introduction** [1]

The focalization of high intensity laser on a solid target produce instantaneous ionization of the irradiated material this is a simple technique to create plasma in the lab. Laser produced plasmas have been studied since the sixties when laser became available as research tools. The plasma characteristics strongly depend by the intensity of incident radiation. There is much interest worldwide in the application of laser matter interaction in laser-confined fusion (ICF) where multiple laser beams are focused on a small target containing the thermonuclear fuel. At present in Europe there is a big program (HIPER) dedicated to the fast ignition (FI) scheme of ICF. In FI the compression and ignition phases are separated: first multiple ns beam compress the target, then a ps laser is focused on the compressed matter generating a intense beam of hot electrons that sparks the thermonuclear ignition. Besides ICF-FI there are several interesting arguments that could be explored through laser matter interaction like the study of matter in extreme conditions of pressure and high density produced by the shock wave generated when the laser hit and ablates the front surface of the solid target, this physics has applications in astrophysics contest also. Another interesting subject is the physics of generation, propagation and absorption of electron and proton beams produced when the laser interacts with matte; this research is relevant to FI but can have also applications in proton Hadrontherapy for the cure of human cancer. The complete description of laser-matter interaction needs whole understanding of different process in different plasmas region and their time evolution. In particular laser energy absorption, the radiative and conductive transport of energy delivered in the absorption zone towards other plasma regions; the plasma hydrodynamics. All of these subjects are strongly interconnected. My thesis work is composed in two parts originating by two different campaign of measurements in various laser facility around the world ( PALS, Prague,Ceck Republik; ILE Osaka, Japan; TIFR Mumbai, India). The first part is focused on the physics of high compressed materials and in particular in the studies of the equation of states-EOS in the pressure range of tens of Mbar. Various target materials are investigated including low-density plastic foam used in the ICF-FI targets. The experiments we performed produced new results for pressure above 3 Mbar that before where not present in the literature.

The second part of my thesis is the study of polarimetric detection of laser induced ultra short magnetic pulses in over dense plasma. The interaction of ultra intense, ultra short laser pulses with solid density materials, leads to extreme states of matter under laboratory conditions. Such tiny and explosively ionized plasmas house the largest and shortest lived magnetic fields on Earth and are important sources of coherent and incoherent electromagnetic radiation, fast ions, and electrons

across a wide energy range. It has been shown both theoretically and experimentally that at high intensities light is absorbed in such a short lived plasma by many collisionless mechanisms such as  $\mathbf{j} \times \mathbf{B}$  heating (ponderomotive acceleration), vacuum heating, and resonance absorption RA resulting in the generation of hot electron currents which are in the form of jets. These jets propagate along the direction of laser axis in case of  $\mathbf{j} \times \mathbf{B}$  heating, while in RA the propagation is along the direction of target normal. The medium, in turn, responds to the hot electron current by setting up an equivalent charge neutralizing return current so that the net current is always below the Alfvén limit. This resultant current generates huge pulses of azimuthal, quasi-static magnetic field whose evolution captures the complex transport of hot electrons through the dense medium. The knowledge of such transport processes is crucial for fast ignition FI scheme of inertial fusion. The success of FI, in fact, depends on the generation of hot electrons, their collimation, transport, and eventual stopping in the over dense region of the plasma. The estimation of hot electron stopping length and factors affecting it, are therefore, extremely important. Various innovative techniques such as measurement of higher harmonic cutoffs and proton radiography have been applied to probe the magnetic field in the overdense region of laser generated plasma, but there have been very few reports on the temporal dynamics of the process with sub picosecond time resolution. In my thesis I present femtosecond time resolved pump-probe polarimetry to decipher the evolution of mega gauss magnetic fields generated near the critical density layer in different types of targets.

# Part 1: EOS of Carbon

## Chapter 1.

### Laser-plasma interaction.

#### 1.1.1 Plasma generation

The interaction of a laser pulse with intensity  $I_L > 10^7$  W/cm<sup>2</sup> with a cold material induces the vaporizations of the first target layers. The ablated material can interact with incident radiation absorbing it and shielding the solid surface according to laser pulse frequency, pulse duration ( $\tau_L$ ) and pulse intensity; therefore the crater depth produced will strongly depend from laser parameters. For short pulses crater will be not too deep. For laser intensities  $I_L > 10^{10}$  W/cm<sup>2</sup> the vaporized material it is also ionized. For more details on ultrashort, intense laser see Appendix 1; for more on laser-plasma interactions see Part 2.

#### 1.1.2 Different plasma regions.

At these laser intensity and for sufficient target thicknesses ( $d > t_L \cdot c_s$ ,  $c_s$  is the sound speed in the material) and target density ( $r > 10^{-2}$  g/cm<sup>3</sup>) the interaction evolves in the following pattern:

Laser light reach the solid surface only at the very beginning of the laser pulse, then the ablated and ionized material expand away from front target surface forming a rarefied and hot cloud. The laser radiation penetrate this rarefied cloud until a region with density close to critical density where laser energy get absorbed; from this absorption layer the energy is transferred to target through thermal conduction and radiative transport that in turn produces further material ablation who accelerates away from target surface toward regions of lower density. Because of this, for momentum conservation, we have the generation of a shock wave that propagates inside the cold target material. See Fig. 1 where the various zones are depicted.

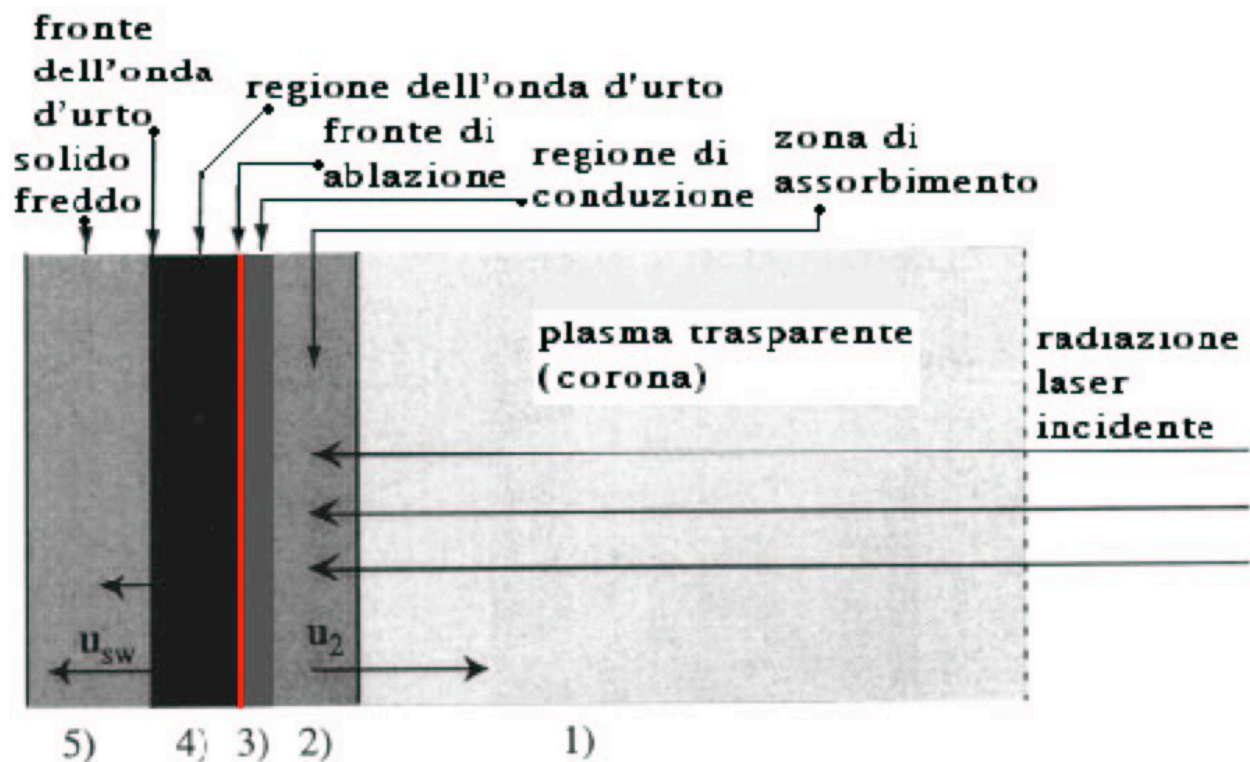


Fig.1.1 Scheme of the evolution of a solid target irradiated by laser.

### 1.1.3 Laser absorption

The absorption of radiation can be of two kinds: collisional or resonant. Collisional absorption is also called “inverse bremsstrahlung” and it is related to plasma free electrons that oscillate in the laser electromagnetic field. For laser fields not too intense the electron dynamics is ruled only by the wave electric field because the effect of the magnetic field is negligible so the electron motion is transversal to laser propagation direction. The electrons transfer their oscillatory energy to ions through elastic collisions that is electrons absorbs continuously energy from the laser field and gives this energy to ions colliding with them. In this way the local ion and electron temperature increase.

The laser wave cannot penetrate beyond the critical surface where the plasma electric density has the critical value:

$$n_{ec} = 1.118 \cdot 10^{15} \text{ m}^{-3} \lambda_0^{-2} \tag{1.1.1}$$

That is when the plasma electron frequency given by:

$$\omega_{pe} = e \sqrt{\frac{n_e}{m_e \epsilon_0}} \quad (1.1.2)$$

And the laser frequency  $\omega_L = 2\pi c/\lambda_0$  ( $\lambda_0$  is the vacuum laser wavelength)

For  $n_e > n_{ec}$ , the plasma index of refraction became imaginary and the waves become evanescent. Collisional absorption becomes very effective for densities close to critical density (slightly less). Resonant absorption is a complex process, and it is connected to the formation of plasma electrostatic waves that are produced when the incident laser wave propagates at an angle oblique into respect to the gradient of electronic density. Laser must also be p polarized (that is the electric field oscillates in the incidence plane that is the plane containing the directions of the gradient of  $n_e$  and the  $k$  vector of laser wave). In proximity of the critical density the plasma index of refraction becomes very small and then the wave electric field becomes very big; here the component of the wave electric field parallel to the gradient of plasma electronic density can resonantly excite plasma wave. Electromagnetic laser energy is absorbed by electrostatic waves; then through several mechanisms (both collisional and not collisional) this energy is at last transferred to electrons increasing their temperature and generating relativistic electron beams that propagate normally inside the target. For some experiments it is possible to reduce the above effects reducing both the laser intensity and wavelength (going to higher harmonics). In this way we can study a collisional only picture of our experiment that is a regime where is bigger the collisional absorption into respect to the resonant one [1,2]. The limit is given by:

$$I_L (\text{W/cm}^2) \cdot \lambda_0 (\mu\text{m}) < 10^{14} \quad (1.1.3)$$

#### 1.1.4 Energy Transfer.

The transfer through the plasma of the energy deposited by the laser can happen in two different ways: thermal conduction and irradiation. The prevalent mechanism is given by electron thermal conduction, that depends strongly by the temperature and by its gradient and it is described by classical theory by Spitzer-Harm [3, 4], that give for the heat flow:

$$\mathbf{q}_{SH} = - K_0 T^{5/2} \nabla T \quad (1.1.4)$$

where  $K_0$  is thermal conductivity. Numerical models from experimental data shows that above formula it is valid only for low heat flows that is for heat flows much less of the free streaming [5, 6]:

$$q_{FS} = n_e K T (K T / m_e)^{1/2} \quad (1.1.5)$$

( $K$  is the Boltzmann constant), that estimates the maximum heat flux that the plasma can carry. In this case the flux is given by the product of (1.1.5) by a coefficient  $f$  that is much less than one ( $f$  = flux limiting factor: 0.03 - 0.1 [7, 8]). Conductive transport gives a bigger contribution into respect irradiation in the energy transfer (this is true for low  $Z$  target material). It is directed mainly toward the bulk of the target but there is a small part is directed toward the external front surface of the target to increase the corona isothermal expansion.

The radiative transport is strongly dependent from the material opacity that decrease increasing radiation frequency. Soft x-ray (low energy) is absorbed and reemitted while is passing through the material, while high energy hard x-rays photons are absorbed once heating locally the material or they pass through the target without interactions [9].

### 1.1.5 Hydrodynamics

The plasma regions, described before, evolves in base of conservation laws of mass momentum and energy described by the following equations [10]:

$$\frac{\partial \rho}{\partial t} + \nabla \cdot (\rho \mathbf{v}) = 0 \quad (1.1.6)$$

$$\frac{\partial \mathbf{v}}{\partial t} + \mathbf{v} \cdot \nabla \mathbf{v} = - \frac{1}{\rho} \nabla P \quad (1.1.7)$$

$$\frac{\partial}{\partial t} \left( \rho u + \frac{\rho v^2}{2} \right) = - \nabla \cdot \left[ \rho \mathbf{v} \left( u + \frac{v^2}{2} \right) + P \mathbf{v} \right] + \rho Q \quad (1.1.8)$$

where  $\rho$ ,  $\mathbf{v}$ ,  $P$  e  $u$  are the density, fluid velocity, pressure and specific internal energy (per mass unity);  $Q$  is the external energy source (per unit volume and time). The corona is characterized by a very high temperature (few KeV) and by a very low density. Corona expansion in vacuum is self similar because the system increase its dimensions but the plasma is distributed always in the same way; and the temperature is almost constant this while the laser pulse is still present; this isothermal behavior of the expansion is possible by a partial flux of heat from the conduction region toward the

exterior. In the conduction zone the profiles of temperature and density have opposite behaviour like it is shown in Fig. 1.2. The plasmas produced from the ablation process are accelerated in the opposite direction of laser radiation propagation; the fluid velocity, in the reference frame of ablation surface, increases with target distance from zero value (on the ablation surface) to sonic values in proximity of the absorption region. The thickness of the conduction zone increases with time. The position of the ablation surface is assumed to be in correspondence of the density of cold solid target (fig 1.2). Beyond this surface we find the shock wave region, where the density is bigger than the one of unperturbed material. The compression ratios increase with shock pressure, but there is a limit that in the approximation of a perfect mono atomic gas is found to be equal to 4. From the thermodynamic point of view the behaviour of a shocked solid material can well be approximated to the one of a perfect gas. This is because when the pressure is very high, also the temperature is very high so that calculating internal energy it is possible to neglect the interactions between the atoms (we have also ionization); therefore atoms and electrons behave like particles in a perfect gas.

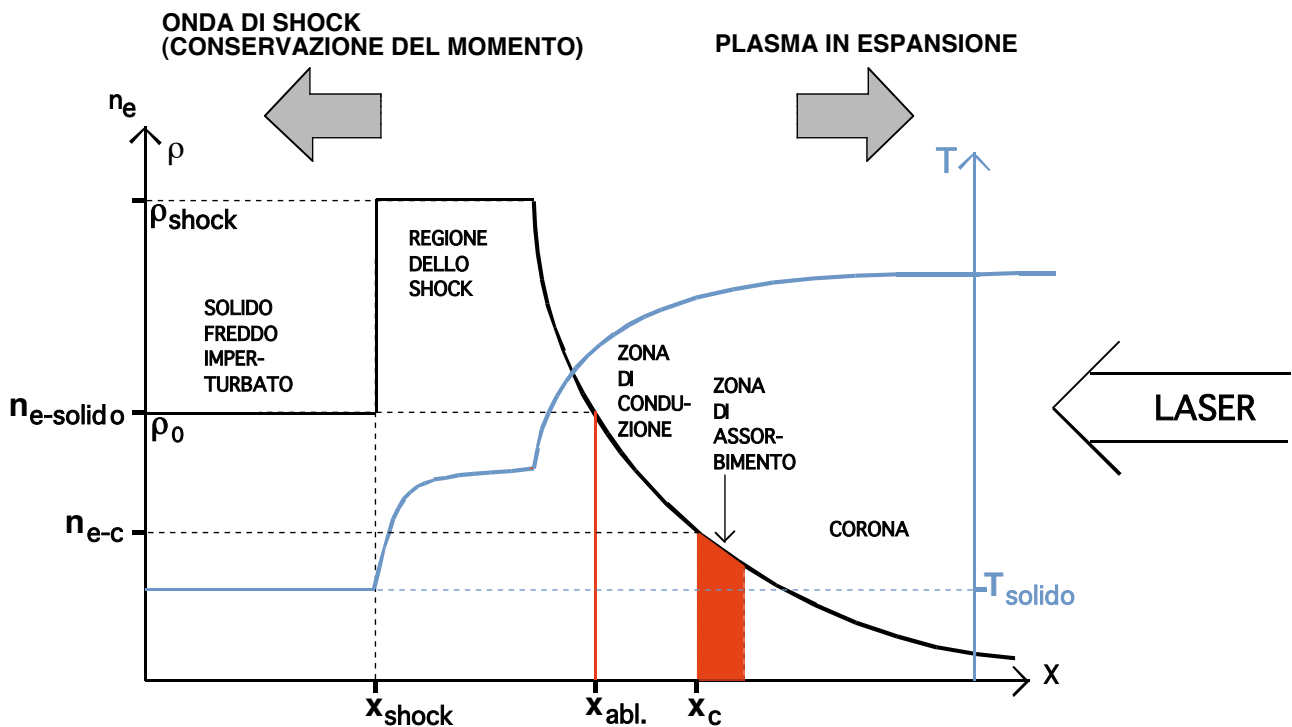


Fig.1.2 Temperature and density profiles in different target regions.

During shock wave evolution the wave front hits the cold material with a supersonic velocity  $U_s$  proportional to the square root of the ratio between the pressure of the compressed  $P$  (behind the wave front) and the density of unperturbed zone  $\rho_0$  (in front of the wave front). The material

invested by the shock wave gain in forward acceleration and acquires a velocity  $U_p$  that is less than  $U_s$ , but it is of the same order of magnitude. The thickness of the zone crossed by the shock wave (compressed zone) is shorter than the original cold material (with a ratio between initial and final densities), besides this thickness increases with time, while the shock wave front moves forward. Assuming that the velocities are constant (neglecting the early on accelerating phase):

$$\Delta X_{(\text{zona compressa})} = \left( U_s - U_p - \frac{dm}{dt dS} \cdot \frac{1}{\rho_0} \right) \cdot t \quad (1.1.9)$$

where  $dm/dtdS$  is the ablation rate (assumed constant), that is the target ablated mass per unit time and unit surface. Also the compression ratio is tied to the velocity and is given by:

$$\frac{\rho}{\rho_0} = \frac{U_s - \frac{dm}{dt dS} \cdot \frac{1}{\rho_0}}{U_s - U_p - \frac{dm}{dt dS} \cdot \frac{1}{\rho_0}} \quad (1.1.10)$$

The velocity associated to ablation rate as in equations (1.1.9) and (1.1.10), that is  $(dm/dtdS)/\rho_0$ , is small in respect to  $U_s$  and  $U_p$ ; therefore it is possible to neglect it and simplify the equations:

$$\Delta X_{(\text{zona compressa})} = (U_s - U_p) \cdot t \quad (1.1.9')$$

$$\frac{\rho}{\rho_0} = \frac{U_s}{U_s - U_p} \quad (1.1.10')$$

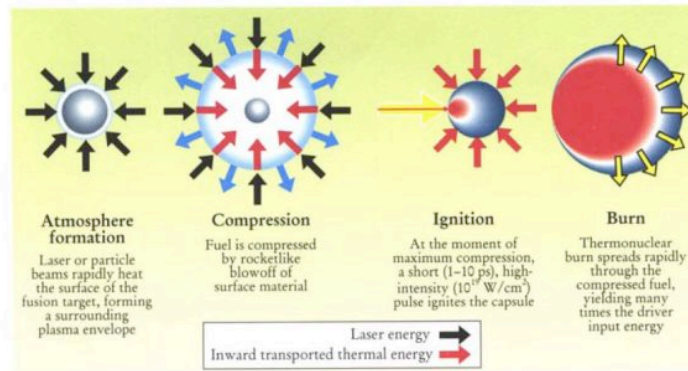
When the shock wave front reaches the rear target surface it heats up the material with the consequent emission of electromagnetic thermal radiation. The hydrodynamics of the rear surface results in vacuum expansion of the last few layers of the accelerated material and also the generation of a relaxation wave reflected back into the compressed material.

### **1.2.1 Inertial Confinement Fusion: ICF [11]**

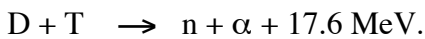
In order to produce nuclear fusion reactions very high levels of temperature and density of the thermonuclear fuel are required; this in order to overcome the coulomb barrier of the interacting nuclei. The ICF scheme uses short powerful laser beams to symmetrically irradiate a small capsule containing the nuclear fuel. The capsule is made of an outer shell of ablating material with a low atomic number (plastic), an inner shell of solid deuterium and tritium (DT) and a core in the gaseous state. The laser pulses ablate the surface this results in the production of a shock wave

propagating toward the centre of the capsule, compressing the nuclear fuel to high densities and high temperature required for fusion reactions. Many synchronized converging laser beams (hundreds) are symmetrically focused on the target surface in order to avoid uneven events [12].

## Fast Ignition of Fusion



The even molar DT mixture is chosen because it has the combustion temperature easier to reach (4.3 KeV). The energy yield is of  $3.4 \cdot 10^{18}$  erg/g. The single fusion process is :



In fig. 1.3 it is shown a typical target scheme.

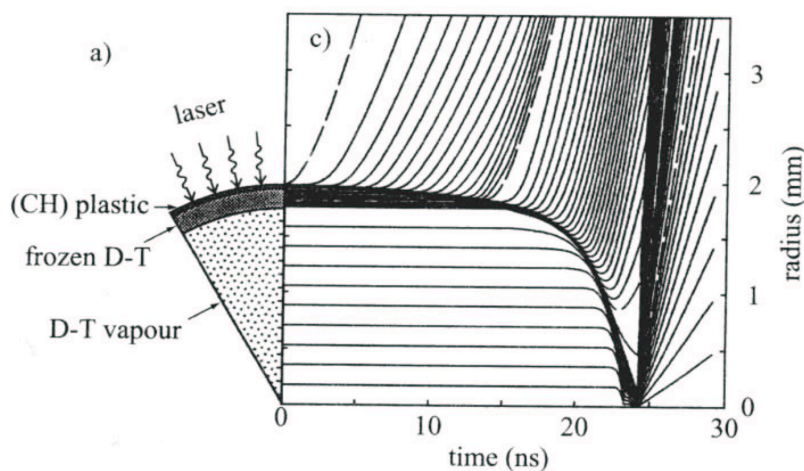
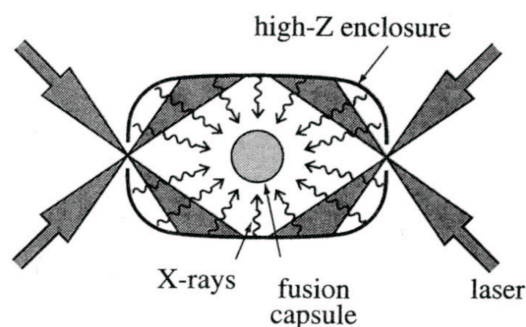


Fig.1.3 ICF target and time evolution under irradiation.

The solid shell, with a radius equal to 1/10 of the total sphere radius (2 mm), has an outer plastic layer and an inner part containing frozen DT nuclear fuel, the core is gaseous. When the multiple laser beams irradiate the outer surface the ablation of the plastic layer begins. Then a hydrodynamic implosion process takes place. The shock wave produced by the ablation penetrates the solid shell layer and accelerates it, then it propagates in the gaseous inner sphere with brisk acceleration to the solid-gas interface. Then it propagates toward the center of the sphere compressing the DT. When the initial wave reaches the interface it generates also a relaxation reflected wave that propagates through the solid material toward the outside, this in turn produces further acceleration of the material toward the inside; when it reaches the ablation surface, it finds the pressure maintained by the laser so it is reflected once again like a centripetal shock wave. This process repeats many times at both surfaces of the solid layer accelerating the material; in this way the portion of the shell not ablated yet behaves like a pusher compressing further the DT. During this sequence of processes a fraction of the laser energy is absorbed and transformed in kinetic energy of the materials that implodes. Calculated values of absorption efficiency are about 80% while the hydrodynamic efficiency is of 10%. Therefore it is about the 8% of the laser energy that is transformed in implosion kinetic energy. At the end of compression the kinetic energy is transformed in thermal energy; the fuel is now confined in a very tiny volume and its hot core (corresponding to some % of the total mass) has reached values of temperature and density that allow the fusion reaction. From the hot core the reaction propagates toward the outside involving all the DT mass. 1000 times the density of solid DT must be reached for fusion. Because initially most of the DT mass is in the shell, this means that the final pellet radius must be about 1/15 of the initial radius. The energy required for this kind of implosion is about  $10^6$  J and the power is on the order of  $10^{14}$  W (this implies laser pulses on the order of 10 ns). There is another scheme to irradiate the target: the indirect irradiating scheme [13] (fig. 1.4); where an Au covered cavity is used in order to have high efficiency production of x-ray.



*Fig.1.4 Indirect irradiating scheme for ICF target.*

The fuel pellet is positioned inside the cavity and the multiple laser beams are made to interact with the cavity walls producing x-rays (like a blackbody). It is this x-ray flow that irradiates the target surface ablating it producing then implosion and ignition. The advantage of this scheme are: better irradiation uniformity with less hydrodynamic instabilities and higher hydrodynamic efficiency; simpler positioning of the target since inside a cavity with uniform radiating field. There is a less energy absorption of the laser energy because before it needs to be transformed in x-ray radiation. Recently a new scheme has been proposed as alternative to ICF: fast ignition (FI) [14]. Basically FI maintain the same scheme of ICF only one new thing is added: when the pellet is in the stage of maximum compression (due to the action of multiple laser beams as explained before) a single high intensity ps laser beam hit along the beam the compressed capsule in a focal spot of some 20  $\mu\text{m}$  on the capsule surface. The interaction of this laser pulse with the plasma surrounding the pellet produces a beam of hot fast electrons that are emitted in the forward direction and heats the core of the imploded capsule and sparks the nuclear fusion reactions that eventually will propagate to all regions.

### **1.2.2 Equations of State: EOS**

In material physics the studies of the properties of compressed matter is very important also in conjunction with ICF. Knowledge in this field is still in its infancy since it is very difficult to realize experimental conditions to get very high pressures (several Mbar), and utilize at the same time accurate diagnostics. Also the theoretical models that describes such processes are very complex and accurate only in some range of the thermodynamic parameters.

Several experimental techniques have been used to reach high pressures in matter. With statical methods [15] it is possible to reach a maximum pressure of 1 Mbar. Dynamical scheme consist in creating a shock wave that propagates into the material and compress it to very high pressures. Various techniques have been used: gas gun, that accelerates a slug to the velocity of several Km/s, toward a solid target [16]; conventional (chemical) explosions [17], that allows to reach some Mbar and nuclear explosions [18], where it is possible to reach very high pressures of some Gbar. Another dynamic technique not based on explosion (which are difficult to realize) is based on the utilization of a power laser to irradiate a solid sample to generate a shock wave. With the power laser available today it is possible to reach pressures of hundred of Mbar. With laser in addition it is possible to obtain experimental data with higher statistic then nuclear explosions.

## **Thomas-Fermi Model.**

The theory of EOS of a highly compressed material follows the model of Thomas-Fermi [10, 19]. According to classical thermodynamics it is sufficient that the temperature is rather high in order to neglect the energy of interaction between the particles respect their kinetic energy in order to treat the material like a perfect gas. Quantum effects becomes important at high level of density while temperature are low. In this case the electron De Broglie wavelength becomes of the same order of the average distance between neighbour particles and the Pauli principle of exclusion becomes important. More if the electronic temperature it is not much bigger then the so called degenerative temperature

$$T_0 = \frac{1}{8} \left( \frac{3}{\pi} \right)^{2/3} \frac{h^2}{m_e k} n_e^{2/3} = 4.35 \cdot 10^{-11} (\text{°K} \cdot \text{cm}^{2/9}) \cdot n_e^{2/3} \quad (1.2.1)$$

The electrons form a degenerative gas and it is required to use the Fermi-Dirac statistic

$$n_e(\varepsilon) \approx \frac{1}{e^{(\varepsilon - \mu)/kT} + 1} \quad (1.2.2)$$

Where  $\varepsilon$  is the electron energy and  $\mu$  is the chemical potential of the electronic gas that depends on the temperature and on the electron density. According to the TF model the plasma is described as a system of nuclei and electrons, there is not difference between free and bound electrons. Nuclei follows Boltzmann statistics and contribute separately to the pressure and to the internal energy of the system. To calculate the electron contribution the gas is pictured as a collections of atomic spherical cells with radius  $r_0 = (3/4\pi n_a)^{1/3}$ , where  $n_a$  is the numerical atomic density. Each cell contain a nucleus and  $Z$  electrons. The energy of each electron is given by:

$\varepsilon = p^2/2m_e - e\phi(r)$ , where  $\phi(r)$  is the coulomb potential. The ionization degree can be found by (1.2.2), finding the number of free electrons, that is with positive energy inside the cell:

$$Z^* = \int_{C = \frac{4}{3}\pi r_0^3} d^3r \int_{\varepsilon > 0} \frac{d^3p}{1 + e^{[(\varepsilon - \mu)/kT]}} \quad (1.2.3)$$

With this method it is not possible to calculate the interaction energy potential between the atoms and the binding energy; the cells are small spheres that interact only pushing one another and repelling in base of their kinetic pressure. Therefore this model could be applied both in the case of high density (where attractive forces are negligible into respect repulsive ones), and high temperature when the potential energy associated to coupling forces are negligible respect the thermal kinetic energy.

**Shock Waves.**

In order to study the EOS through shock waves we need to know the main characteristics of such waves. A shock wave is generated from the evolution of a sound wave, that is characterized by an adiabatic material compression who propagates at the sound velocity  $c$  given by:

$$c = \left( \frac{\partial P}{\partial \rho} \right)_S^{1/2} \quad \left[ = \left( \gamma \frac{P}{\rho} \right)^{1/2} = \left( \gamma \cdot \text{cost} \cdot \rho^{\gamma-1} \right)^{1/2} = \left( \gamma \cdot \text{cost} \cdot P^{1-1/\gamma} \right)^{1/2}, \text{ nel caso di GP} \right] \quad (1.2.4)$$

In fig. 1.5 it is shown the profile of a compression wave. In normal acoustic waves the perturbation is very small, that is  $\Delta P = (P_1 - P_0) \ll P_0$ ; therefore in the propagation the profile will not be deformed. Instead for intense and fast perturbation ( $\Delta P \approx P_0$  o  $\Delta P \gg P_0$ ) where already the initial profile is very steep, the wave alter the shape because the portion of the wave characterized by a higher pressure propagates at a higher speed (equation 1.2.4) respect the wave portion of the lower part of the profile where the pressure is lower. In such situation the profile becomes almost vertical at the wave front (fig. 1.5b), this becomes a discontinuity surface for the material thermodynamic variables; the result of this extreme deformation is the shock wave.

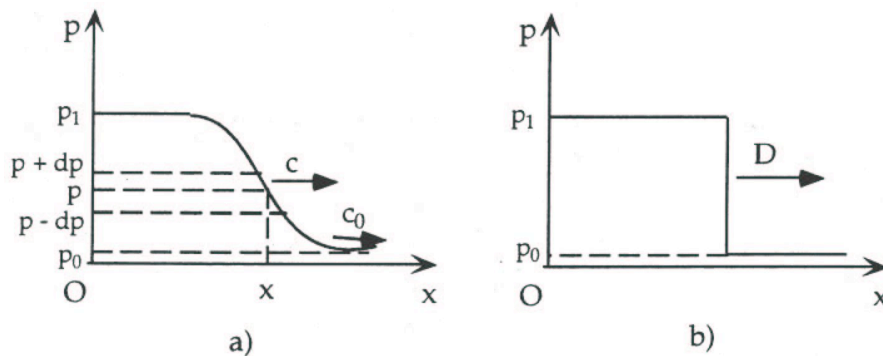


*Fig.1.5 Compression and shock waves.*

The shock wave dynamics is ruled by Rankine-Hugoniot equations, that contains the conservation of mass, momentum and energy across the shock wave front. For unidimensional system they are:

$$\rho_0 D = (D - v)\rho \quad (1.2.5a)$$

$$P - P_0 = \rho_0 D v \quad (1.2.5b)$$

$$\left[ u - u_0 + \frac{1}{2} v^2 \right] \rho_0 D = P v \quad (1.2.5c)$$

where "D" and "v" are the shock velocity and fluid velocity respectively. Fluid velocity is the velocity of the accelerated material; "u" is the internal specific energy. Pressure, density and internal specific energy have an index "0" when referred to the unperturbed material in front of the shock wave and no index when referred to material compressed by the shock. To represent the fluid under the action of the shock wave we can imagine that the shock wave is produced by a piston that push forward the material at a speed v and applying a pressure P. Reproducing situations with different values of P, we obtain different values of  $\rho$ , that grows with P; if in a plane P, $\rho$  (or P,V, where  $V = 1/\rho$  is the specific volume) we join different points matching the material compressed by the shock, we obtain a Hugoniot, that is steeper than the correspondent adiabatic curve (that start from the same initial point parte  $P_0, \rho_0$ ), like it is shown in fig. 1.6. The Hugoniot does not represent a true transformation and for a given pressure P the system jumps directly from the initial state point  $P_0, \rho_0$  to the final one P, $\rho$  missing all the intermediate state points, that is this kind of compression is irreversible. The work done from the piston on the fluid is,  $L = P \cdot (1/\rho_0 - 1/\rho)$ , is converted in internal energy,  $(u - u_0)$ , and in kinetic energy,  $v^2/2$ :

$$\frac{v^2}{2} = \frac{1}{2} (P - P_0) \cdot \left( 1/\rho_0 - 1/\rho \right) \quad (1.2.6)$$

therefore by difference of (1.2.6) respect L, the increment of internal energy will be:

$$u - u_0 = \frac{1}{2} (P + P_0) \cdot \left( 1/\rho_0 - 1/\rho \right) \quad (1.2.7)$$

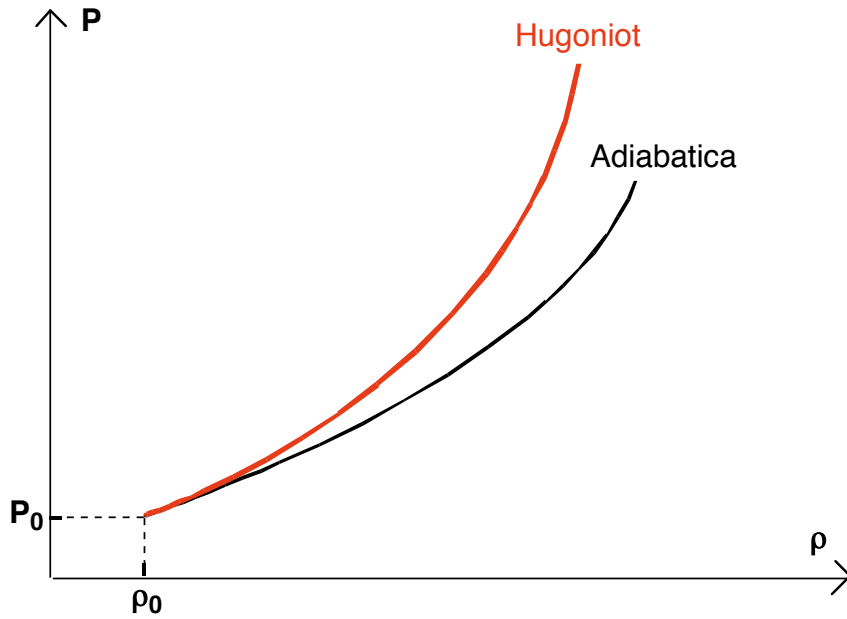


Fig.1.6 Hugoniot curve in the plane  $P, \rho$ .

From previous equations in the limit of strong shocks, ( $P \gg P_0$ ) we obtain:

$$P \approx \rho_0 D v \quad (1.2.5b')$$

$$u - u_0 \approx \frac{v^2}{2} \approx \frac{1}{2} P \left( \frac{1}{\rho_0} - \frac{1}{\rho} \right) \quad (1.2.5c')$$

In the case of a perfect gas (GP), it is possible to obtain in analytical form all the shock wave hydrodynamics relations. The Hugoniot, results in the  $P, \rho$  plane:

$$P = \left[ \frac{(\gamma + 1)/\rho_0 - (\gamma - 1)/\rho}{(\gamma + 1)/\rho - (\gamma - 1)/\rho_0} \right] P_0 \quad (1.2.8)$$

while the "polar of shock" (the Hugoniot in the plane  $P, v$  instead of the plane  $P, \rho$ ) and the shock wave velocity are given by:

$$v = \left( \frac{2}{\rho_0} \right)^{1/2} \cdot \frac{(P - P_0)}{[(\gamma - 1)P_0 + (\gamma + 1)P]^{1/2}} \quad (1.2.9)$$

$$D = \left\{ \frac{1}{2\rho_0} [(\gamma - 1)P_0 + (\gamma + 1)P] \right\}^{1/2} \quad (1.2.10)$$

that for strong shocks becomes:

$$P = \frac{(\gamma + 1)\rho_0}{2} v^2 \quad (1.2.9')$$

$$D = \left[ \frac{(\gamma + 1) P}{2 \rho_0} \right]^{1/2} \quad (1.2.10')$$

### **Impedence Mismatch Method**

To find a point in the EOS of a compressed material, that is the correspondent state point after being hit by the shock wave we need to use equations (1.2.5) and we need to measure experimentally two quantity. We have 3 equations and 5 parameters of the compressed material:  $v$ ,  $D$ ,  $u$ ,  $\rho$ ,  $P$ ; it is assumed that we know the parameters of the unperturbed cold material. In this way it will be possible to obtain 3 thermodynamic parameters.  $u$ ,  $P$ ,  $\rho$ . Temperature remains undetermined and we need to measure it in an independent way. The experimental measurement of 2 of the 5 parameters it is not an easy task and require sophisticated diagnostics. The only parameter that it is easy to measure is the shock velocity. We used a double target composed by a reference material of which we know the EOS and by a second material with unknown EOS. Experimentally it is necessary only to measure the velocity  $D$  in both materials. This is known as the “impedence mismatch” method and we will show how to obtain  $\rho$ ,  $P$ ,  $u$  for the unknown material. We assume that the first target layer is the reference material that is usually aluminium Al; second layer is the material under study that we indicate with X. When the shock wave produced in the first Al layer reach the Al-X interface we have a discontinuity and two waves are produced: the first is a progressive shock that propagates in the X material; the other is a reflected wave back into the Al and will be again a shock wave if  $\rho_{0X} > \rho_{0Al}$  or a relaxation wave if  $\rho_{0X} < \rho_{0Al}$  (corresponding to an adiabatic transformation). If we consider the case  $\rho_{0X} < \rho_{0Al}$ , the shock wave transmitted in X is characterized by a lower pressure and a bigger fluid velocity into respect the primary wave in the Al. In fig. 1.7 it is shown the pressure across the interface just before (a), and just after (b), the original shock wave reach the separation surface. The equilibrium conditions and the mass continuity, impose that after interface reflections we have same pressure and fluid velocity in both materials (that is  $P$  and  $v$  of the transmitted shock wave and of the relaxation reflected wave must be the same). Considering the  $P, v$  diagram in fig. 1.8, we observe that, for strong shock, the measurement of  $D$  in the Al allow to find through (1.2.5.b'), the point A on the shock polar of cold Al (curve 1), this point represent the state reached by the Al after the passage of the shock. The relaxation wave reflected back into the Al lead the material to a state B that correspond to a point in the relaxation adiabatic that cross A (line 3).

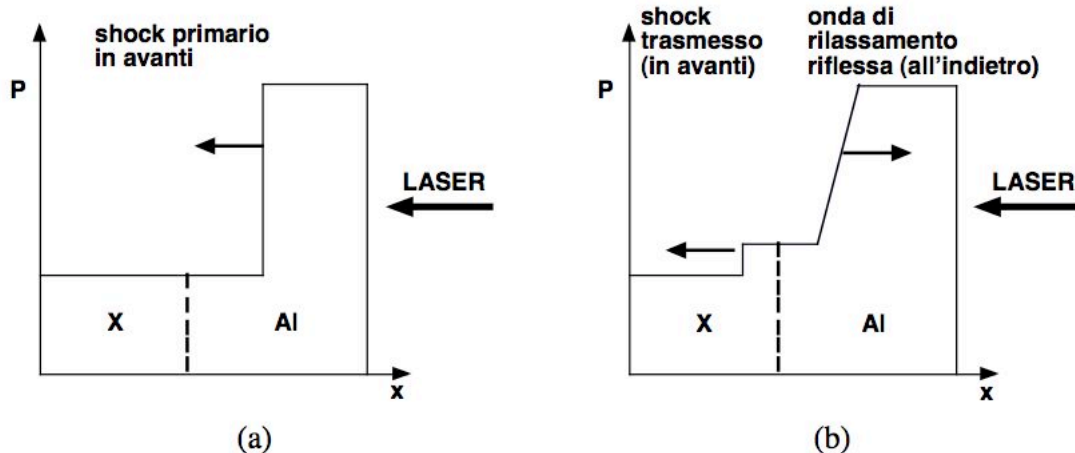


Fig.1.7 Transmission and reflection of the primary shock wave at the interface between the reference material (Al) and the material under study (X), for the case  $\rho_{0X} < \rho_{0Al}$ .

This point can be found measuring  $D$  in the material X, and using (1.2.5.b');  $P$  e  $v$  must be equal in the relaxed Al as well in the compressed X material, therefore the line  $P = \rho_{0X} D_X v$ , that must cross in a point the shock polar of the cold material X, must also cross (in the same point B) the relaxation curve of the Al. In the case  $\rho_{0X} > \rho_{0Al}$ , the slope of the line  $P = \rho_{0X} D_X v$  is more steep respect the line  $P = \rho_{0Al} D_{Al} v$ , and we should have considered its intersection B with the curve 2, that represent the states that can be reached by the Al following a second compression (second shock wave), that follows the one that led to the state A. This second shock polar of Al (curve 2) is decreasing in the  $P, v$ ; this because  $v$  in the plot is the fluid velocity respect the laboratory, while the

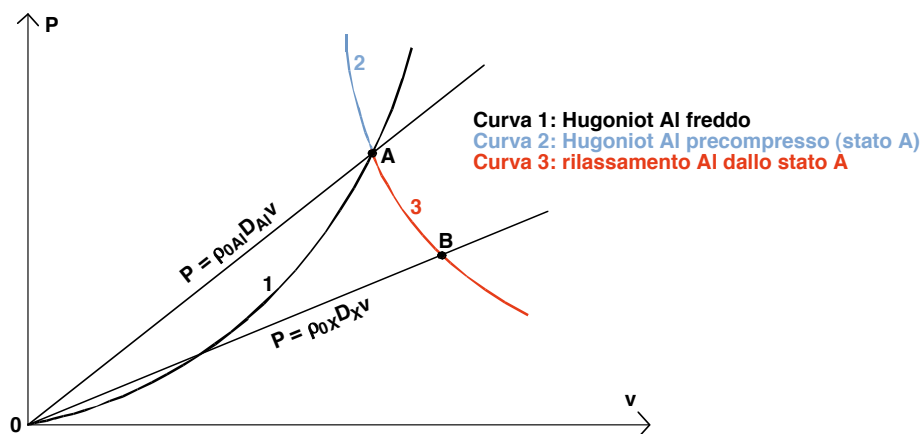
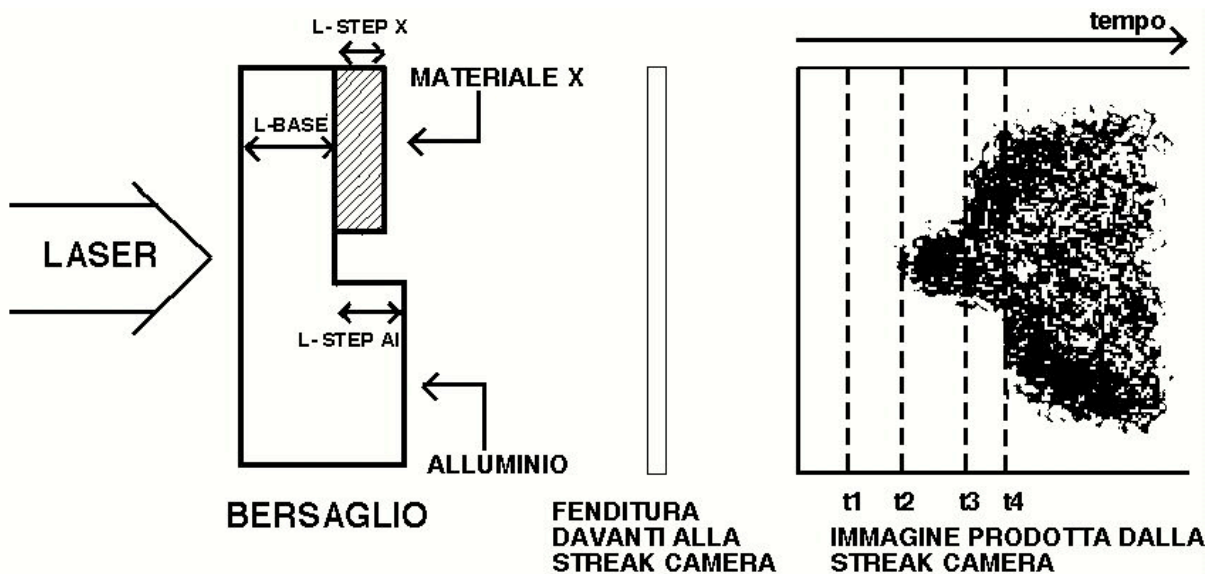
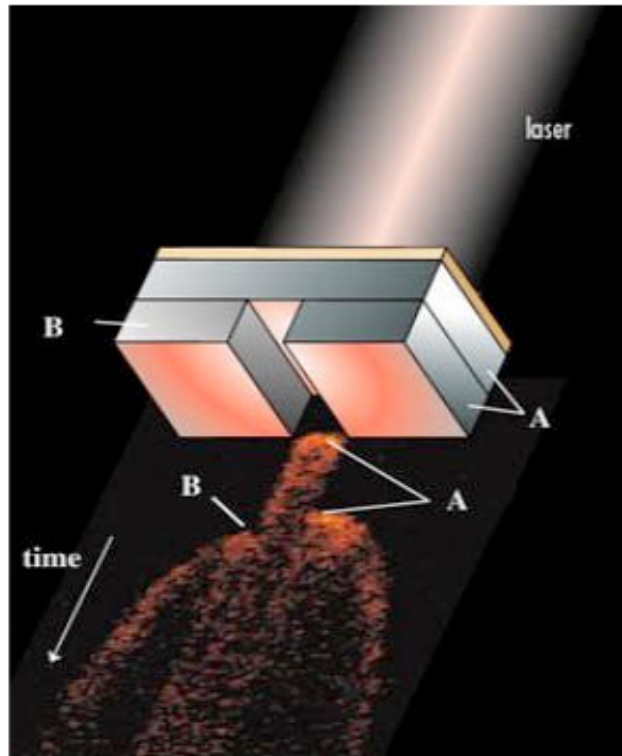


Fig.1.8 Impedence Mismatch Method to find EOS in the material X: shock polar for cold Al and for compressed Al and the relaxation adiabat for the Al.

fluid velocity in the polar shock where  $P(v)$  is increasing (see equation 1.2.9', in the case of perfect gas), is the velocity of the material invested by the new shock wave respect the material in front of it, that is:  $v_2' = v_2 - v_1$ , where 1 is the situation after the passage of the first shock. While 2 after the second shock and with the apex we refer velocities to the new reference system. We know the EOS of the Al therefore we can reconstruct the curve 1 and 2, or 1 and 3, that we need in order to apply this method. Therefore with the measure of  $D_{Al}$  and of  $D_X$  we can find  $v$  and  $P$  of the compressed material X (the coordinates of the point B); through equations (1.2.5) we find at the end the parameters  $\rho$  and  $u$ . Streak cameras are used experimentally to measure  $D$ . This diagnostic is positioned in such a way to observe the rear target surface; and it is coupled to a CCD. The output is a time and space resolved image of the thermal radiation emitted by the rear target surface that it briskly heats up when reached by the shock wave (see fig.19). In many experiment we used double step targets as shown in fig. 1.9. They are built with a first base layer of Al where are positioned two steps: one of Al and the other one of the material X.





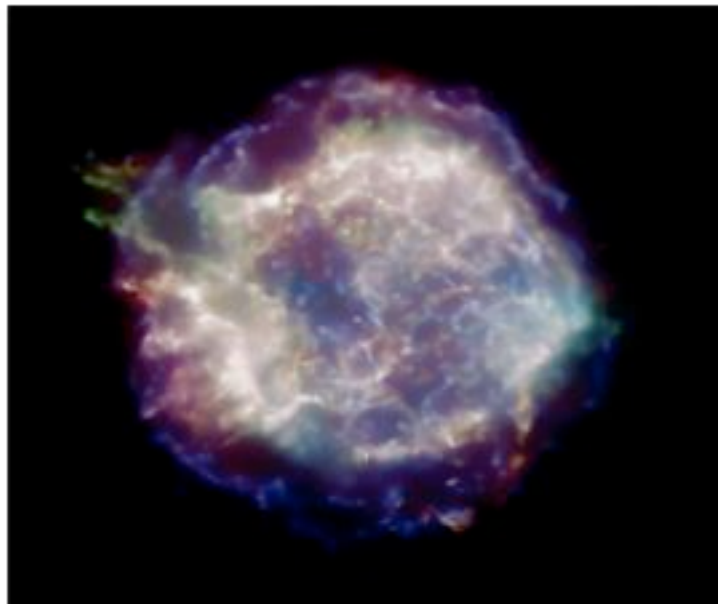
*Fig.1.9 Double step target and record of streak camera image.*

In this way, with the same laser shot, it is possible to measure the shock wave arrival times at target rear surface in correspondance of the base, the Al step and the X step; and we find easily the velocities  $D_{Al}$  and  $D_X$ . It is necessary to use also the Al step because the dynamic of the shock wave at early stage in the Al base goes through an acceleration phase and also because the Al step is a useful reference in the streak camera image. For EOS of highly compressed materials there exist numerical tables containing informations for some materials. The most accurate tables are the SESAME tables prepared at the Los Alamos laboratories. These tables are based on experimental datas and on theoretical models of different kinds according to the range of applications of temperature and density. SESAME tables contains datas for 150 different materials. The tables represent the pressure  $P$  and the internal specific energy  $E$  as a function of the density  $\rho$  and of the temperature  $T$ . For some materials there exist datas also for phase transitions (fusion and vaporization). Typically the intervals of density and temperature are respectively  $10^{-6} - 10^4 \text{ g/cm}^3$  and  $0 - 10^5 \text{ eV}$ . There are also SESAME tables for the opacity and conductivity of several materials. EOS tables are then realized using combination of different theoretical models chosen in order to obtain datas that match experimental results. Thomas-Fermi-Dirac theory is used for the electronic thermal contribution to EOS, while the ionic contribution is described with Debye theory in the solid phase and with Lindemann formula at fusion point, while above this change of phase an

interpolation is applied. This interpolation brings the material toward the behaviour of an ideal gas in the regime of high temperatures.

### **1.2.3 Astrophysic.**

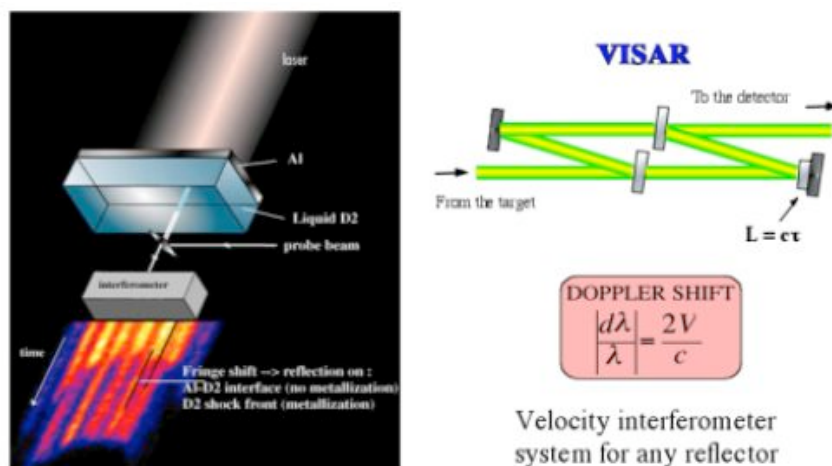
Astrophysics is linked to plasma physics; the stellar objects are made of plasmas with different densities and temperatures. In particular some phenomena connected with the hydrodynamics and to the radiative transport of the energy are important in order to understand some phases of the stellar evolutions. In the laboratory it is possible to reproduce to a very small scale such conditions with plasmas created by laser. Therefore the laser plasma interaction represents a useful tool to test models that describe particular astrophysical phenomena. EOS and material opacity becomes then very useful informations in the astrophysical contest. An interesting field of study is the shock wave generated during supernovae explosions, shock waves that propagate radially towards the outer regions where reaches material with a density profile decreasing with  $r$ .



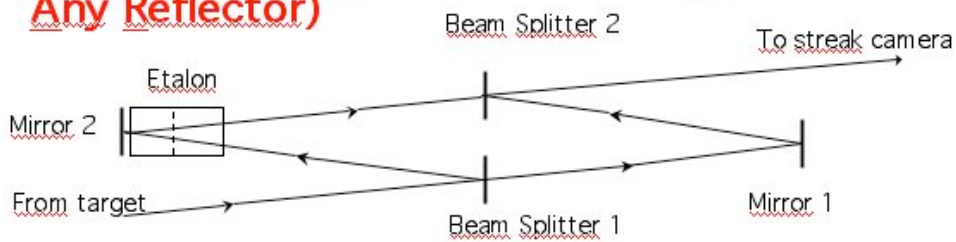
Remnant of Cassiopea A supernova, pictured in X at Chandra observatory

As we have seen above in 1.2.2, this disuniformity in the medium lead in the shock wave region to a pressure decrease with consequent increase of fluid and shock velocity and of the temperature. This process can represent an important acceleration mechanism for the material that will be ejected in the exterior space from the exploding star. In this way it is possible also to explain the emission of very short X-ray and UV burst from low-density external plasma regions when compressed and heated to very high temperature by shock wave. There exist several theoretical and experimental

works on this subject [22,23,24,25] and in particular some of laser-plasma interaction to study the impact of a high velocity flux of material with a low density steady material. This kind of experiment are of interest to simulate in small laboratory scale supernova explosions, where high velocity expelled material impact with surrounding rarefied material leading to hydrodynamics phenomena that could explain the characteristics of “supernova remnants”. Also in planetology there are situations where the field of laser-produced plasma can give its contribution. One example is given by the odd Uranus magnetic field [26,27], characterized by an eccentric axis of symmetry (respect the body of the planet) and also by an unusual high intensity. To explain datas collected by Voyager 2 mission, one hypothesis given is that the source of the magnetic field is located in the planet mantle and not in the nucleous. The core is reach of iron while the mantle is reach of water, ammonia and methan. To explain the presence of a conducting material inside the mantle one possible explanation is that at the very high pressures present in the mantle the methan through pirolisis separates the carbon from the hydrogen and that the carbon goes through a phase transition leading to a metallic state. This could be one contribution but we need to report that recent experiment shows that also water goes through a phase transition into a conducting state. Therefore it is very important to understand the behaviour of carbon at very high pressure [28 - 37]. We performed recently several experiments in order to understand the phase transition of carbon; in particular at ILE laboratory Osaka Japan we used a set up to measure change of reflectivity of rear carbon target surface under high shock pressure generated by intense laser beams. Reflectivity measurement of rear carbon target shows sharp increase of luminosity after shock compress carbon material, this is indication of phase transition to metallic state. Streak camera picture below show an indication of carbon phase transition coupled to an increase of reflectivity under high pressure shock. In the pictures above it is shown the scheme for VISAR measurement.



## VISAR (Velocity Interferometric System for Any Reflector)



$$\delta = \frac{2h}{c} \left( n - \frac{1}{n} \right)$$

Delay introduced by etalon

$$\frac{v_0 - v}{v} = \frac{2V}{c}$$

Doppler Shift

$$F(t) = \frac{v_0 - v}{v_0 v} c \delta$$

Fringe displacement

$$V(t) = \frac{\delta}{2\delta} \frac{F(t)}{(1 + \Delta)}$$

$$\Delta = 1 - \left( \frac{n_0}{n_0^2 - 1} \right) v_0 \left. \frac{dv}{dv} \right|_{v=v_0}$$

### 1.3 Experimental problems

Laser-plasma interaction studies present several experimental difficulties that must be overcome in order to really understand the physics we are studying. In what follows we show some of these problems and the techniques used in recent years, with the help of new technologies, in order to solve them.

#### 1.3.1 Laser disuniformities

With the (limited power) lasers available in the '80ties in order to achieve high intensities on target ( $I > 10^{14} \text{ W/cm}^2$ ) to produce high pressures in the irradiated material ( $> 1 \text{ Mbar}$ ) it was necessary to build experimental set ups in which the front target surface was very close to the converging lens focus. In this way the laser energy was concentrated in very small focal spot ( $< 100 \mu\text{m}$ ). Also although the laser intensity radial profile before the lens ("near field") is flat, the lens focalization creates an intensity Gaussian profile in correspondance to the focus. Finally the diffraction process that undergoes the coherent laser radiation during its propagation and in the focalization step in the end give rises to local over intensities ("speckles") in correspondance of the focal spot. Their dimensions and distances are of the order of a few micrometers.

#### 1.3.2 Optical omogeneization techniques

The presence of local sovraintensities in the focalized laser profile leads to several problems that can deteriorate the quality of hydrodinamical phenomenaproduced in the laser-plasma interaction.

To improve this situation since the early '80 laser beams optical omogeneization techniques have been developed. These are based on the breaking of spatial/temporal coherence because is just the coherence that makes different beams zones to interfere in the focal spot to produce sovraintensities (hot spot). Random phase plate (RPP) and phased zone plate (PZP) are the recent devices.

### **Random phase plate**

A random phase plate consist of a transparent substrate with a resin patterned top deposition. The pattern consist of small squares of dimension about 1 mm. These regions impose to laser radiation a phase shift of 0 or  $\pi$ , according to the random surface distribution the laser pass through. This phase plate is positioned just behind the focalizing lens. In the focal plane, that usually coincide with the target surface, we obtain an intensity distribution that is very irregular on a small scale characterized by spikes distributed randomly with dimension and separation on the order of  $\lambda f/D$ , where f and D are the lens focal and the beam diameter before focalization. The envelope of this profile is similar to the diffraction image of a square aperture, that is  $I(x) \sim \text{sinc}^2(\pi x d/\lambda f)$ , that is close to a gaussian, where x is the distance from the axis of the beam along a parallel direction to a square side of the structures engraved on the RPP. The first order minimum is localized at  $x = \lambda f/d$  and contains the '82% of the whole energy. Basically breaking the spatial coherence we get an intensity profile that still contains a multitude of spikes but the spatial scale now is much smaller on the order of a few  $\mu\text{m}$  ( $\lambda f/D$ ). This situation is much improved one respect no RPP because small scale intensity disuniformities are levelled hydrodinamicly by transversal thermal conduction (perpendicular to laser axis) that is localized in the conduction zone. Disuniformities localized in the absorption zone are smoothed while the energy is transferred to the ablation surface, where it is applied the pressure that sustain the shock wave, also because their distance is small into respect the electrons average free path

**Phased zone plate.** Phased zone plate (PZP) have been recently used to improve optical omogeneization techniques of laser beams. A PZP consist of a circular plate where with lithography techniques are engraved on one side a set of Fresnel lenses all with equal dimension. A Fresnel lens is made of a sequence of circular zones with alternate opaques and transparent behaviour giving a phase shift of 0 and  $\pi$  to incident laser radiation.

## Principle of Optical Smoothing

### Phase Zone Plate => Flat top Intensity distribution

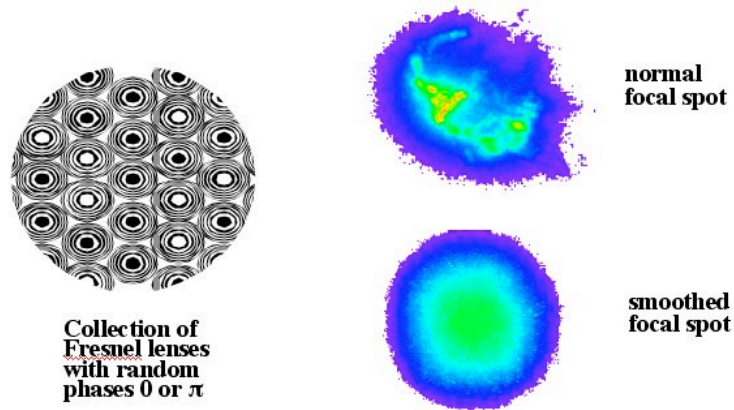


Fig.1.16 Fresnel lens distribution in a phase zone plate (PZP).

Each Fresnel lens is characterized by a focal  $f$ , which determines also the radius of circular zones .

If we indicate with  $R_n$  the external radius of the  $n^{\text{th}}$  circular zone we get for each  $n$ :

$$f = \frac{R_n^2}{n\lambda} \quad (1.3.1)$$

PZP plate is positioned behind the focal lens. This combined optical system has a focal  $f_{\text{tot}}$  :

$$\frac{1}{f_{\text{tot}}} = \frac{1}{f} + \frac{1}{f_L} \quad (1.3.2)$$

where  $L$  indicates the principal lens. Being  $f \gg f_L$ , we get  $f_{\text{tot}} \approx f_L$ . In the focal plane every single Fresnel lens focalizes the radiation in different spots as shown in fig.1.17.

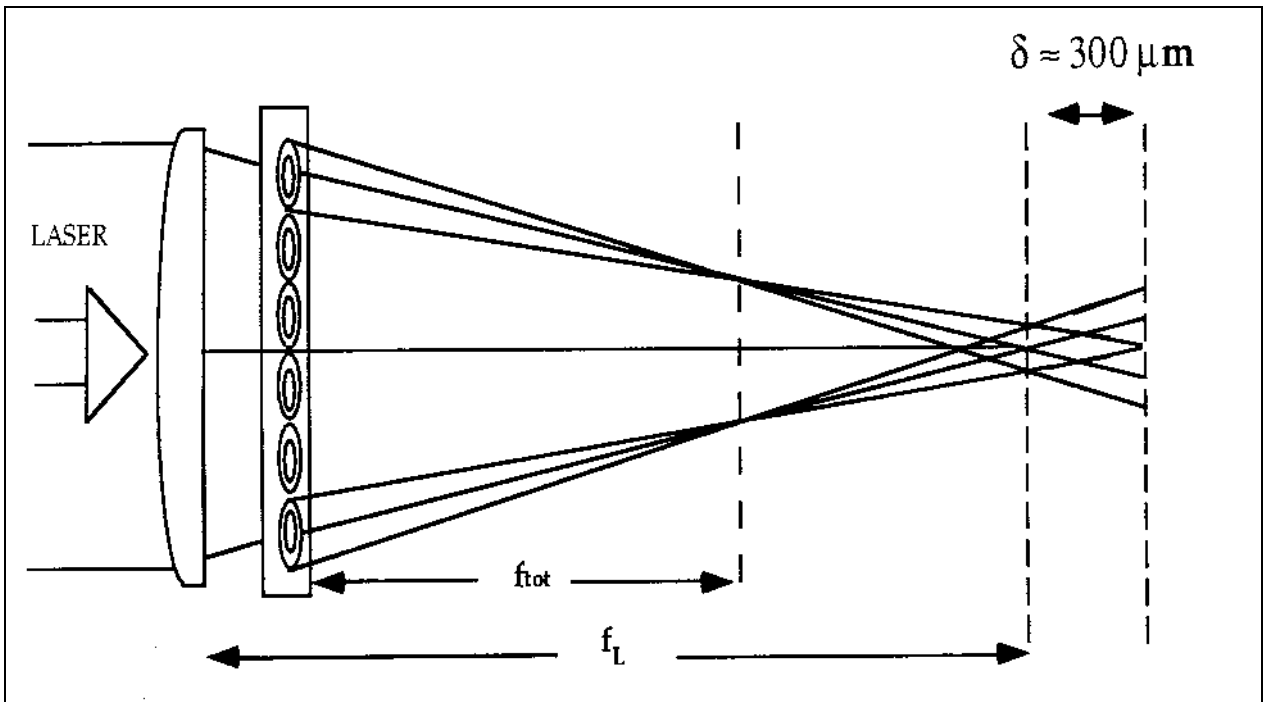


Fig.1.17 Optical system "principal lens-PZP". Is indicated the focal plane of the lens, and also of the optical system and the best defocalized position for the target surface.

PZP gives a super Gaussian flat top distribution for the intensity. The spikes hot spot are smoothed out by thermal electron conduction.

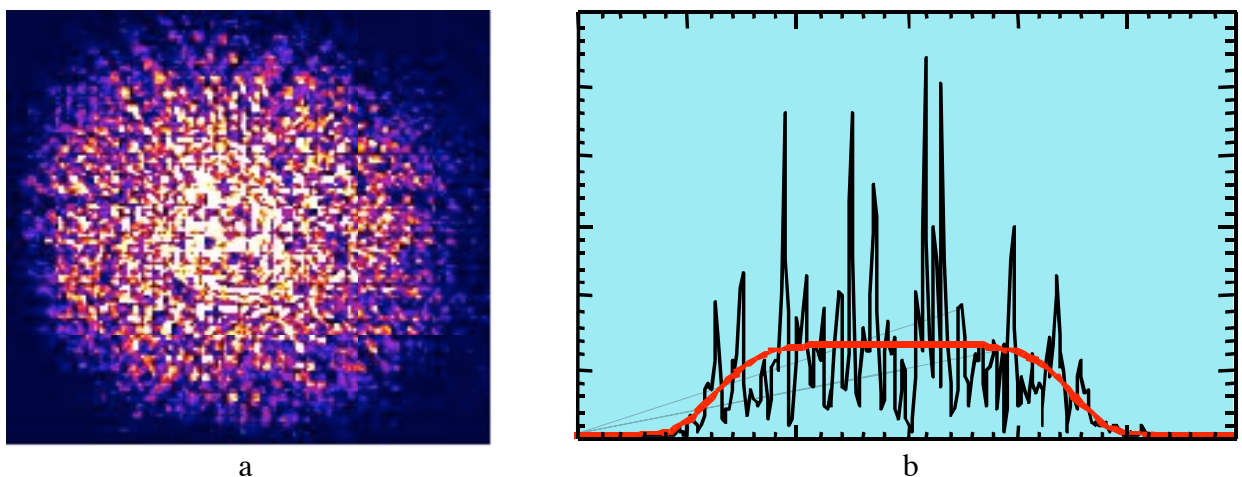
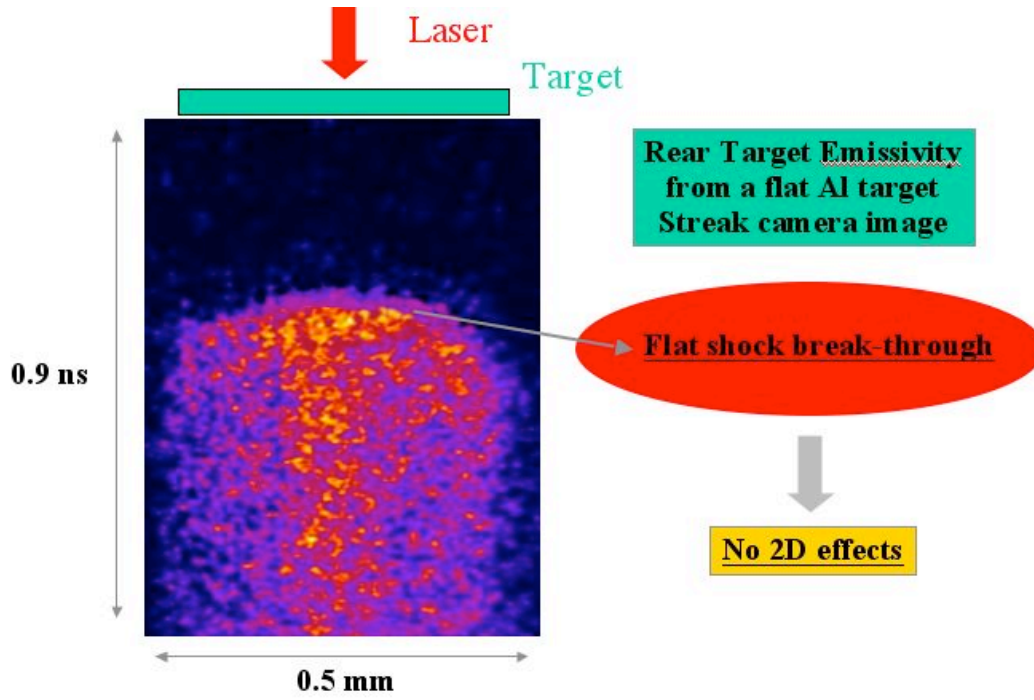


Fig.1.18 Laser Intensity as given by the lens-PZP system on the defocalized plane: a) 2D image; b) Intensity profile  $I(r)$ ; below streak images shows flat top profile due to uniform shock.



### Ablation pressure

The ablation process leads to the formation of the shock wave that is produced by the plasma expansion into vacuum. The study of the plasma expansion is treated as an hydrodynamical problem of a fluid that is electrically neutral (this because plasma is neutral). It is possible then to obtain scaling laws for the ablation pressure  $P_a$  (that is the same as the shock pressure) and for the mass ablation rate,  $d(m_a)/dt$ . In our experimental situation we have, on target, max laser intensity  $I \sim 10^{14} \text{ W/cm}^2$  and we are in the case of delocalized absorption in wich laser radiation is absorbed mainly in the plasma corona, before it reaches the critical density zone. In this regime the ablation pressure,  $P_a$ , and the mass ablation rate,  $d(m_a)/dt$ , are given by:

$$P_a(\text{Mbar}) \approx 11.6 \left( \frac{I_L(\text{W/cm}^2)}{10^{14}} \right)^{\frac{3}{4}} \lambda(\mu\text{m})^{-\frac{1}{4}} \left( \frac{A}{2Z} \right)^{\frac{7}{16}} \left( \frac{Z^*}{3.5} \right)^{-\frac{1}{8}} \tau(\text{ns})^{-\frac{1}{8}}$$

$$\dot{m}_a \left( \frac{\text{kg}}{\text{cm}^2\text{s}} \right) \approx 143 \left( \frac{I_L(\text{W/cm}^2)}{10^{14}} \right)^{\frac{3}{4}} \lambda(\mu\text{m})^{-\frac{1}{2}} \left( \frac{A}{2Z} \right)^{\frac{2}{8}} \left( \frac{Z^*}{3.5} \right)^{-\frac{1}{4}} \tau(\text{ns})^{-\frac{1}{4}}$$

## **Streak cameras operating principle**

The streak camera is a device to measure ultra-fast phenomena and delivers intensity vs. time vs; position (or wavelength) information. It's name dates back to the early days of the high speed rotating drum cameras. These cameras would "streak" reflected light onto film. No other instruments which directly detect ultra-fast light phenomena have better temporal resolution than streak camera. Since the streak camera is a two dimensional device it can be used to detect several tens of different light channels simultaneously. For example used in combination with a spectroscope time variation of the incidence light intensity with respect to wavelength can be measured (time resolved spectroscopy). Used in combination with proper optics it is possible to measure time variation of the incident light with respect to position (time and space-resolved measurement). Fig.1 shows the operating principle of the streak camera. The light being measured passes through a slit and is formed by the optics into a slit image on the photocathode of the streak tube. At this point four optical pulses which vary slightly in terms of both time and space and which have different optical intensities are input through the slit and arrive at the photocathode. The incident light on the photocathode is converted into a number of electrons proportional to the intensity of the light so that these four optical pulses are converted sequentially into electrons. They then pass through a pair of accelerating electrodes where they are accelerated and bombarded against a phosphor screen. As the electrons produced from the four optical pulses pass between a pair of sweep electrodes high voltage is applied to the sweep electrodes at a timing synchronized to the incident light (see Fig.2). This initiates a highspeed sweep (the electrons are swept from top to bottom). During the high-speed sweep the electrons, which arrive at slightly different times are deflected in slightly different angles in the vertical direction and enter the MCP (micro channel plate). As the electrons pass the MCP they are multiplied several thousands of times after which they impact against a phosphor screen where they are converted again into light. On the phosphor screen the phosphor image corresponding to the optical pulse which was the earliest to arrive is placed in the uppermost position with the other images being arranged in sequential order from top to bottom, in other words, the vertical direction on the phosphor screen serve as the time axis. Also the brightness of the various phosphor images is proportional to the intensity of the respective incident optical pulses. The position in the horizontal direction of the phosphor image corresponds to the horizontal location of the incident light. In this way the streak camera can be used to convert changes in the temporal and spatial light intensity of the light being measured into an image showing the brightness distribution on the phosphor screen. We can thus find the optical intensity from the phosphor image and the time and incident light position from the location of the phosphor image.

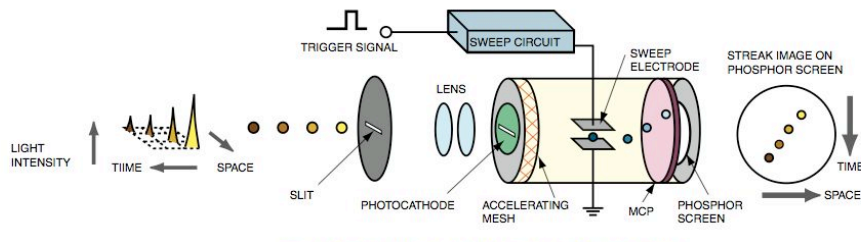


**Fig.1 Operating Principle of the Streak Tube**

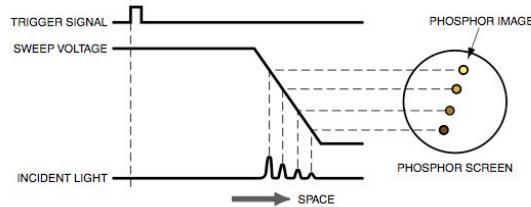


**Fig.2 Operation Timing (at time of sweep)**

**System configuration**

In order to measure ultra-high speed optical phenomena using a streak camera a trigger section and a readout section are required. The basic configuration of this system is shown below.

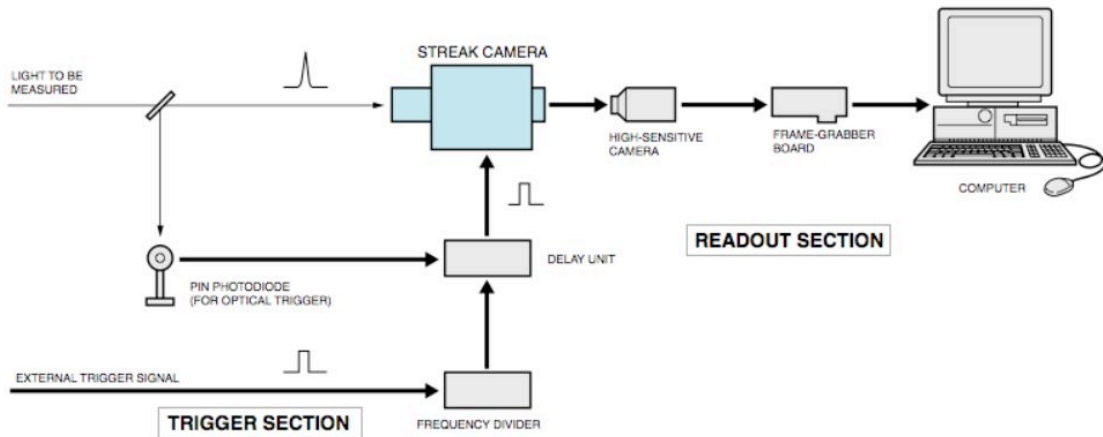


**Fig.3 Basic System Configuration of Streak Camera**

The trigger section controls the timing of the streak sweep. This section must be adjusted so that a streak sweep is initiated when the light being measured arrives at the streak camera. For this purpose we use a delay unit which controls how long the trigger signal which initiates the streak sweep is delayed. A PIN diode is used when the trigger signal is produced from the light being measured.

## **BIBLIOGRAPHY Part 1 Chapter 1**

- [1] C. Garban-Labaune, E. Fabre, C. Max, J. Virmont *et al.*: "Rapport d'activité du groupement de recherches coordonnées Interaction Laser-Matière", Ecole Polytechnique.
- [2] E. Fabre, F. Amiranoff, R. Fabbro, C. Garban-Labaune *et al.*: "Plasma Physics and Controlled nuclear Fusion research", vol. II-IAEA-CN-38/I-4 (IAEA, Vienna) (1980).
- [3] L. Spitzer and R. Härm: "Transport Phenomena in a Completely Ionized Gas", *Physical Review*, 89, 5, pp.977-981 (1953).
- [4] R. S. Cohen, L. Spitzer and P. McR. Routly: "The electrical Conductivity of an Ionized Gas", *Physical Review*, 80, 2, p. 230-238 (1950).
- [5] A. R. Bell: "Laser Produced Plasmas" pp.319-337 in *Plasma Physics - An Introductory Course*, edited by R. Dendy, Culham Laboratory Abingdon, Oxfordshire - Cambridge University Press 1993.
- [6] F. Strati: "Sviluppo di un codice lagrangiano 2D per l'interpretazione di esperimenti sulla propagazione di shock in laser-plasmi", tesi di laurea - Università degli Studi di Milano, (1997).
- [7] W. C. Mead, E. M. Campbell, K. G. Estabrook, R. E. Turner, W. L. Kruer, P. H. Y. Lee, B. Pruett, V. C. Rupert, K. G. Tirsell, G. L. Stradling, F. Ze, C. E. Max, and M. D. Rosen: "Laser-Plasma Interactions at 0.53  $\mu\text{m}$  for Disk Targets of Varying Z", *Phys. Rev. Lett.* 47, pp.1289-1292 (1981).
- [8] T. J. Goldsack, J. D. Kilkenny, B. J. MacGowan, P. F. Cunningham, C. L. S. Lewis, M. H. Key, P. T. Rumsby: "Evidence for large heat fluxes from the mass ablation rate of laser-irradiated spherical targets", *Physics of Fluids*, 25, 9, pp. 1634-1643 (1982).
- [9] R. Sigel: "Laser-Induced Radiation Hydrodynamics and X-ray Generation", in "Laser Plasma Interactions 5: Inertial Confinement Fusion: Proceedings of the Forty Fifth Scottish Universities Summer School in Physics", St. Andrews, Maureen Brett Hooper Ed., p.79, (1994).
- [10] Ya. B. Zel'dovich and Yu. P. Raizer: *Physics of Shock Waves and High-Temperature Hydrodynamic Phenomena*, Edited by Wallace D. Hayes and Ronald F. Probstein, Dover Publications, INC., Mineola, New York (2002).
- [11] J. J. Duderstadt, G. A. Moses: *Inertial Confinement Fusion*, John Wiley & Sons, (1982).

- [12] C. Yamanaka: "Inertial confinement fusion research by GEKKO XII glass laser", *Fusion Technology* ; Vol/Issue: 8:1; 6. Topical meeting on the technology of fusion energy; 3 Mar 1985; San Francisco, CA, USA.
- [13] J. Lindl: "Development of the indirect-drive approach to inertial confinement fusion and the target physics basis for ignition and gain", *Physics of Plasmas*, 2, 11, pp. 3933-4024, (1995).
- [14] M. Tabak, J. Hammer, M. E. Glinsky, W. L. Kruer, S. C. Wilks, J. Woodworth, E. M. Campbell, M. D. Perry, R. J. Mason: "Ignition and high gain with ultrapowerful lasers", *Physics of Plasmas*, 1, 5, pp. 1626-1634 (1994).
- [15] A. Jayaraman: "Diamond anvil cell and high pressure investigations", *Rev. Mod. Phys.*, (1983).
- [16] [http://en.wikipedia.org/wiki/Light\\_gas\\_gun](http://en.wikipedia.org/wiki/Light_gas_gun).
- [17] P. Elias, R. Courchinoux, M. Legrand, N. Toque: "Instability development at the interfaces of explosive-shocked metallic plates", 3rd Intern. Workshop on "The Physics of Compressible Turbulent Mixing", Abbey of Royaumont (France), June 17-19, (1991).
- [18] C. E. Ragan, B. C. Diven, M. Rich, E. E. Robinson, and W. A. Teasdale: "Shock Compression Measurements at Pressures > 1 TPa", *AIP Conference Proceedings*, 78, 1, pp. 169-173, (1982).
- [19] R. M. More: "Atomic physics in inertial confinement fusion", UCRL- 84991, Part I and II, PREPRINT, Lawrence Livermore Laboratory, (1981).
- [20] A. Benuzzi-Mounaix, M. Koenig, G. Huser, B. Faral, D. Batani, E. Henry, M. Tomasini, B. Marchet, T.A. Hall, M. Boustie, Th. De Rességuier, M. Hallouin, F. Guyot, D. Andraut, Th. Charpin: "Absolute Equation of State measurements of iron using laser driven shocks", *Physics of Plasmas*, 9, 6, pp. 2466-2469, (2002).
- [21] A. V. Bushman, I. V. Lomonosov and K. V. Khishchenko, V. P. Kopyshchev, E. A. Kuzmenkov, V. E. Kogan, P. R. Levashov, I. N. Lomov, Pavel R. Levashov: <http://teos.ficp.ac.ru/rusbank/>
- [22] R. Teyssier, D. Ryutov, B. Remington: "Accelerating shock waves in a laser-produced density gradient", *Astrophysical Journal, Suppl. Ser.*, 127, pp. 503-508, (2000).
- [23] M. Koenig, A. Benuzzi-Mounaix, F. Philippe, B. Faral, D. Batani, T. A. Hall, N. Grandjouan, W. Nazarov, J. P. Chieze, R. Teyssier: "Laser driven shock wave acceleration experiments using plastic foams", *Appl. Phys. Lett.*, 75, 19, pp. 3026-3028, (1999).
- [24] D. Batani, A. Balducci, W. Nazarov, T. Löwer, T. Hall, M. Koenig, B. Faral, A. Benuzzi, M. Temporal: "Use of low-density foams as pressure amplifiers in equation-of-state experiments with laser-driven shock waves", *Phys. Rev. E*, 63, 046410, (2001).
- [25] R. P. Drake, S. G. Glendinning, Kent Estabrook, B. A. Remington, Richard McCray, R. J. Wallace, L. J. Suter, T. B. Smith, J. J. Carroll, R. A. London, E. Liang: "Observation of

Forward Shocks and Stagnated Ejecta Driven by High-Energy-Density Plasma Flow", *Phys. Rev. Lett.*, 81, 10, pp. 2068-2071, (1998).

[26] S. Stanley & J. Bloxham: "Convective-region geometry as the cause of Uranus' and Neptune's unusual magnetic fields", *Nature*, 428, p. 151, (2004).

[27] C. T. Russel and J.G.Luhmann: *Encyclopedia of Planetary Sciences*, edited by J. H. Shirley and R. W. Fainbridge, 863-864, Chapman and Hall, New York, 1997.

[28] D. Batani, F. Strati, H. Stabile, M. Tomasini, G. Lucchini, A. Ravasio, M. Koenig, A. Benuzzi-Mounaix, H. Nishimura, Y. Ochi, J. Ullschmied, J. Skala, B. Kralikova, M. Pfeifer, Ch. Kadlec, T. Mocek, A. Pra'g, T. Hall, P. Milani, E. Barborini, P. Piseri: "Hugoniot Data for Carbon at Megabar Pressures", *Phys. Rev. Lett.*, 92, 6, 065503, (2004).

[29] M. Tomasini: "Studio dell'equazione di stato di materiali di interesse astrofisico nel range del Megabar", tesi di laurea - Università degli Studi di Milano, (2001).

[30] C. Olivotto: "Studio dell'equazione di stato del carbonio ad alte pressioni", tesi di laurea - Università di Milano Bicocca, (2002).

[31] H. Nagao, K. G. Nakamura, K. Kondo, N. Ozaki, K. Takamatsu, T. Ono, T. Shiota, D. Ichinose, K. A. Tanaka, K. Wakabayashi, K. Okada, M. Yoshida, M. Nakai, K. Nagai, K. Shigemori, T. Sakaiya, K. Otani: "Hugoniot measurement of diamond under laser shock compression up to 2 TPa", *Phys. Plasmas*, 13, 052705, (2006).

[32] K. Shigemori: "Towards Metallization of Carbon by Strong Shock Compression with Intense Laser", *Review of High Pressure Science and Technology*, 16, 3, pp. 243-250, (2006).

[33] S. Skupsky and K. Lee: "Uniformity of energy deposition for laser driven fusion", *J. Appl. Phys.*, 54, 7, pp. 3662-3671, (1983).

[34] S. Atzeni: "Hydrodynamic instabilities in laser-produced plasmas", *Conference Proceedings*, 88, "Atoms and Plasmas in Super-Intense Laser Fields", pp. 35-64, Edited by D. Batani, C. J. Joachain and S. Martellucci, SIF, (2004).

[35] C. S. Liu, M. N. Rosenbluth, R. B. White: "Raman and Brillouin scattering of electromagnetic waves in inhomogeneous plasmas", *Physics of Fluids*, 17, 6, pp. 1211-1219, (1974).

[36] W. L. Kruer: *Physics of Laser Plasma Interactions*, Addison-Wesley, Redwood City, (1988).

[37] A. Benuzzi, M. Koenig, B. Faral, J. Krishnan, and F. Pisani, D. Batani, S. Bossi, and D. Beretta, T. Hall and S. Ellwi, S. Hüller, J. Honrubia, N. Grandjouan: "Preheating study by reflectivity measurements in laser-driven shocks", *Physics of Plasmas*, 5, 6, PP. 2410-2420, (1998).

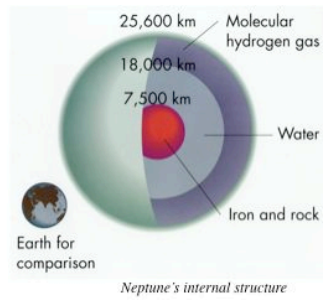
# PART 1

## CHAPTER 2

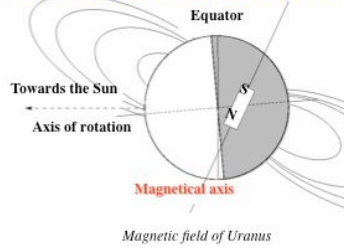
### MEASUREMENT OF CARBON EOS

#### Introduction

We present an experimental point for the carbon equation of state (EOS) at megabar pressures, obtained by laser-driven shock waves. The rear side emissivity of “two-materials two-steps” target (Al-C) was recorded with space and time resolution and, by applying the impedance mismatch method, allowed a direct determination of relative EOS points. Experiments were performed at PALS and LULI laboratories, using carbon samples with two different values of initial density, in order to explore a wider region of the phase diagram. Previously unreachable pressures were obtained. The results are compared with previous experiments and with available theoretical models and seem to show a high compressibility of carbon at megabar pressures. The equation of state (EOS) of carbon at high pressures (megabar or multi megabar regime) is of interest for several branches of physics. Material science: Carbon is a unique element due to its polymorphism and the complexity and variety of its state phases. The EOS of carbon has been the subject of several recent important experimental and theoretical scientific works [1–15]. The important phenomenon of carbon metallization at high pressure has long been predicted theoretically but until now never experimentally proved. At very high pressures the regime of nonideal strongly correlated and partially degenerate plasmas is approached, which is characterized by an almost complete absence of experimental data [15–18]. Astrophysics: The description of high-pressure phases is essential for developing realistic models of planets and stars [19, 20]. As was shown in chapter one, Carbon is a major constituent (through methane and carbon dioxide) of giant planets such as Uranus and Neptune. High pressures are thought to produce methane pyrolysis with a separation of the carbon phase and the possible formation of a diamond or metallic layer [21–23].

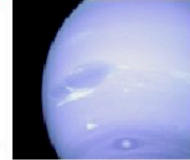


### High magnetic fields measured by Voyager 2

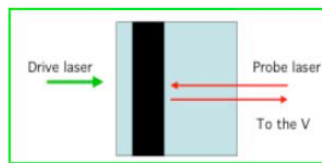


- Mantle of Uranus and Neptune = «hot ices» of  $H_2O$ ,  $NH_3$ ,  $CH_4$
- Intense, assymetrical magnetic field

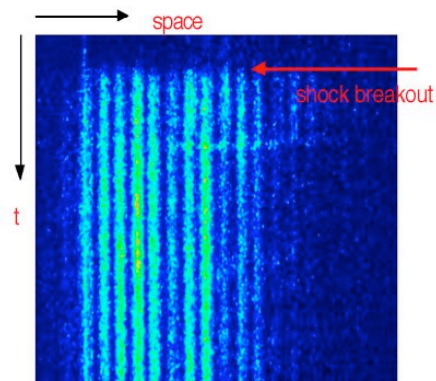
Pyrolysis of methane and separation of carbon?  
 Metallic liquid carbon or diamond layer?  
 Existence of a **fluid, conducting** region (based on water and carbon)?



### Measurements of carbon phase change



**Visar image show sharp  
 Increase in target reflectivity  
 at shock breakout**



C 22 $\mu$ m/LiF,  $d = 0.36 \text{ g/cm}^3$   
 $I_w, I - 770 \text{ J}, 6 \text{ ns}, \text{spot size } 1,5 \text{ mm}$

The picture above show recent results from experiment performed at ILE-Osaka, Japan. From Visar streak image it is evident an increase of reflectivity as high shock wave pressure compress carbon film. This is an indication of a phase transition toward a metallic state for carbon.

Metallization of the carbon layer in the mantle of these planets (the “ice layers”) could give a high electrical conductivity and, by the dynamo effect, be the source of the observed large magnetic fields [24, 25]. Concerning carbon metallization, the first theoretical estimates (Van Vechten [1]) set the triple point for the transition among diamond ( $\alpha$ ), liquid metal ( $\beta$ l), and solid metal ( $\beta$ s) at 1.7

Mbar and 3100 K, a prediction not in agreement with experimental results by Shaner *et al.* [2] and Grover [3]. More recent works set the metallic transition at much larger pressures: Yin and Cohen [4] predict a transition from diamond to a BC-8 semi metallic phase at about 11 Mbar (and a second transition to a SC-4 metallic phase at about 27 Mbar), in fair agreement with the calculations by Biswas *et al.* [5], who put the upper limit of diamond stability at about 12 Mbar, and with the calculations by Fahy and Louie [6] (at about 11.1 Mbar). Ruoff and Luo [7], working on experimental data on gap closure by Mao *et al.* [8], put the metallic transition at about 8.4 Mbar. Such pressures can easily be generated in the laboratory by using laser-driven shocks. At higher temperatures, liquid phases are predicted, going from non metallic at low pressures to semi metallic and metallic as the pressure is increased. The first experimental evidence of a liquid metallic phase was given by Bundy [9]. Nowadays, the most accepted phase diagram of carbon by Grumbach and Martin [10] sets the structural changes in liquid carbon at pressures of 4 and 10 Mbar. This suggests that laser-driven shocks ( $P= 2-6$  Mbar,  $T>20\ 000$  K) should reach a liquid metallic phase.

### **2.1.1 Grumbach - Martin phase diagram**

In Fig.2.1 we report a simplified version of the Grumbach - Martin phase diagram to which we added the Hugoniot curves corresponding to the initial densities  $\rho_0 = 1.6$  and  $1.45$  g/cm<sup>3</sup> (the two values used in our experiment).

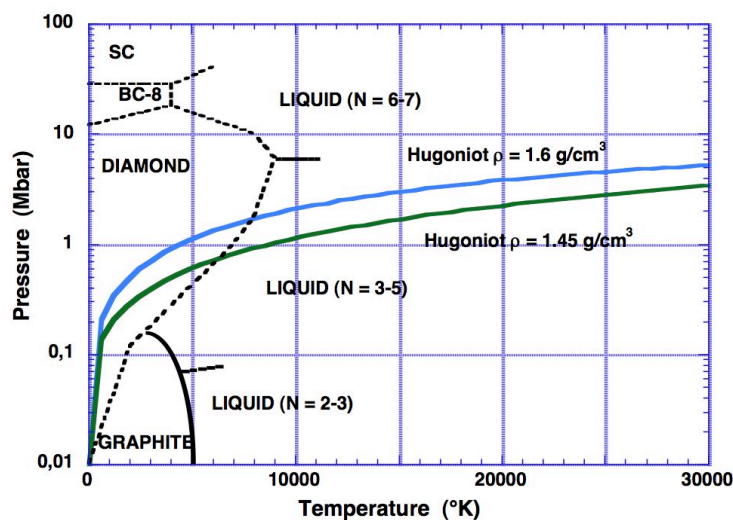


Fig. 2.1. Grumbach and Martin's phase diagram (after [12]) and the two Hugoniot curves corresponding to the initial densities  $\rho_0 = 1.6$  and  $1.45$  g/cm<sup>3</sup>

Again, the liquid metallic phases can easily be reached with laser shocks. These are, indeed, nowadays the only laboratory tool which can achieve pressures of a few tens of megabars [18]. In this chapter i present the first Hugoniot data for carbon that our group obtained with laser- driven shocks. In recent years, it has been well established that laser shocks are a useful tool for high-pressure physics, to compress materials at megabar pressures and measure their EOS [26,27]. The goal of our experiment was to begin the exploration of carbon EOS in the pressure range 1–15 Mbar. We got the first experimental points at pressures higher than 8 Mbar. Moreover, we substantially increased the number of EOS data for carbon at pressures >1 Mbar: nine new EOS points against a total of about 20 points which were available in literature [28–32]. One general limitation of shock-wave EOS experiments is that only data on the Hugoniot curve of the material are obtained. This is due to the fact that shocks compress and heat the material at the same time, so pressure and temperature are no longer independent variables. One way to overcome this limitation is to use a sample with reduced density  $\rho$  (porous or foam target). This changes the initial conditions in the material so that data along different Hugoniot curves are obtained. Hence, by changing  $\rho_0$  the whole EOS plane can be explored. In particular, by reducing the initial density  $\rho_0$  of the sample, the same shock pressure  $P$  will correspond to a higher temperature  $T$  (internal energy  $E$ ) and a reduced final density. The experiment is based on generating high-quality shocks and using “two-steps–two-materials” targets. Relative EOS data of “unknown” materials (here C) are obtained by using a “well-known” reference (here Al). Al behavior at high pressure is well understood, making it a typical reference material for shock experiments [27]. Some laser shots were done at LULI, where three laser beams at  $\lambda = 0.53 \mu\text{m}$  were focused at intensities  $I \approx 5 \times 10^{13} \text{ W/cm}^2$ . The pulse was Gaussian in time with a full width at half maximum (FWHM) of 600 ps.

### **2.1.2 PALS laser and experimental set up**

In order to increase laser energy (and shock pressure), other shots were done with the PALS iodine laser [33], (Fig. 2.2, Fig.2.3, Fig.2.4). with typical energy of 250 J per pulse at a wavelength of 0.44  $\mu\text{m}$ , focused up to an intensity of  $2 \times 10^{14} \text{ W/cm}^2$ . The pulse was Gaussian with a FWHM of 450 ps. In both cases, large focal spots and Phase Zone Plates (PZP) [26] were used to get uniform laser illumination and avoid 2D effects in the propagation of the shock.



*Fig. 2.2 ASTERIX laser at PALS.*

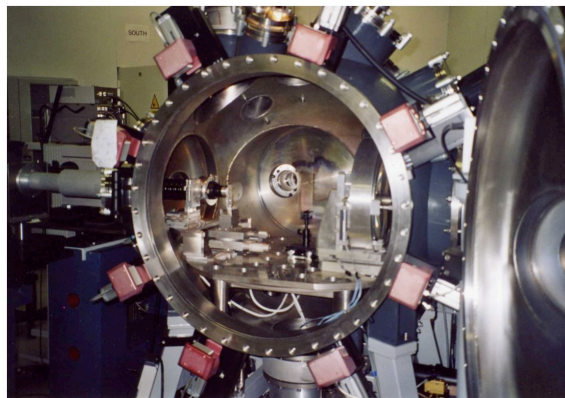


*Fig. 2.3 Spherical interaction chamber at PALS. Laser coming from right is focalized on target by a lens inside the chamber. Light emitted by target is focalized on streak camera (chamber left side).*

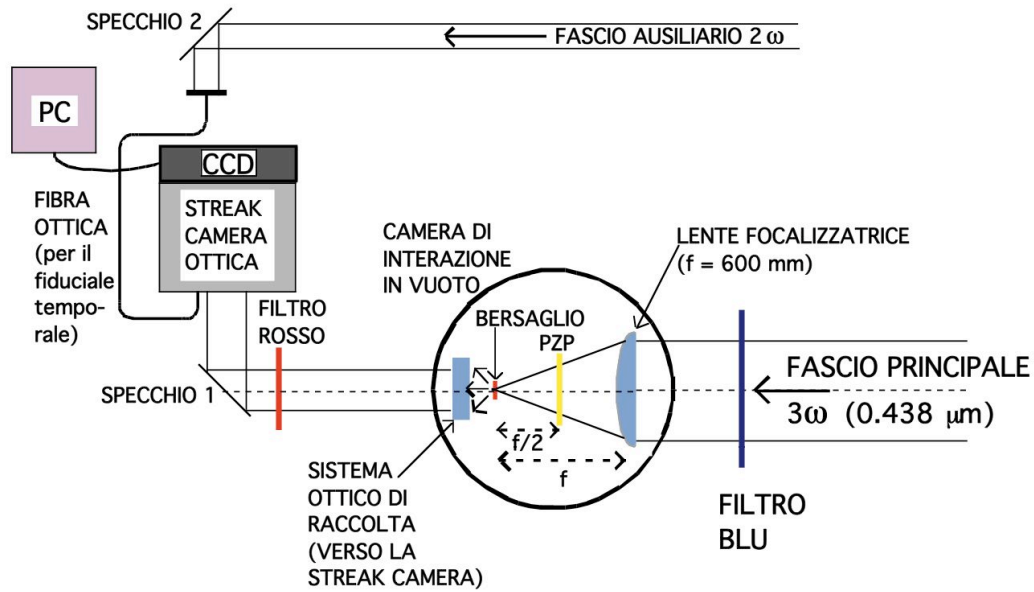


Fig. 2.4 PALS Experimental set-up.

Two diagnostic systems, based on streak cameras coupled to photographic lenses and 12-bit CCD cameras, were used: (a) rear-side time-resolved imaging (to record target self-emissivity), and, (b) time-resolved visible reflectometry (at LULI only). Both diagnostic methods allow the measurements of the shock breakout times from the base and steps of the “two-steps-two-materials” target, Fig. 2.5.

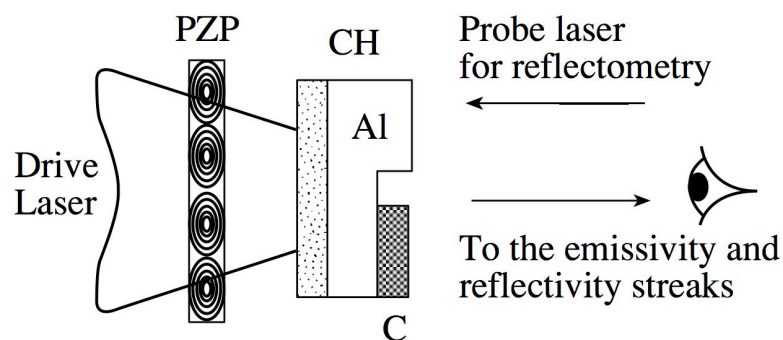


Fig. 2.5 Scheme of the experimental set-up.

The CH layer may be (or may be not) present in order to reduce X-ray emission from laser irradiated side. The probe laser, used at LULI only, was a Nd:YAG converted to  $2\omega$  with pulse duration of 8 ns. Hence, we measured the shock velocity in Al and C simultaneously on the same

laser shot. Details of the experimental set-up are reported in [34] for PALS, and in [26] for LULI (and for the reflectivity diagnostics in [35]). The time and spatial resolution of both diagnostics, in both laboratories, were typical of the order of 10 ps and 10  $\mu\text{m}$ . The reflectivity temporal behavior is important since it can provide evidence of insulator-to-metal transitions (optical reflectivity is directly related to the density of free charge carriers in the material [35]). However this requires a different target configuration, and no attempt was made in this direction in this first experiment.

### **2.1.3 Carbon Targets**

#### **Supersonic Cluster Beam deposition**

Targets, and in particular the carbon layers, are an important part of the experiment. Some carbon depositions were done at the University of Milan (see Fig. 2.8) using the Supersonic Cluster Beam Deposition (SCBD) technique with appropriate masks [36], which allows quite uniform layers and steep steps to be deposited. This particular deposition system allows carbon to stick on Al, avoiding usual de-lamination problems. More importantly, it is possible to deposit carbon layers with densities variable between 1 and 2  $\text{g/cm}^3$ . In our experiment, carbon layers with initial density  $\rho_0 = 1.45 \pm 0.10 \text{ g/cm}^3$  were used. The deposition technique gives an error comparable to the typical  $\leq 5\%$  due to the streak-camera resolution. The Al step thickness was 5  $\mu\text{m}$ .

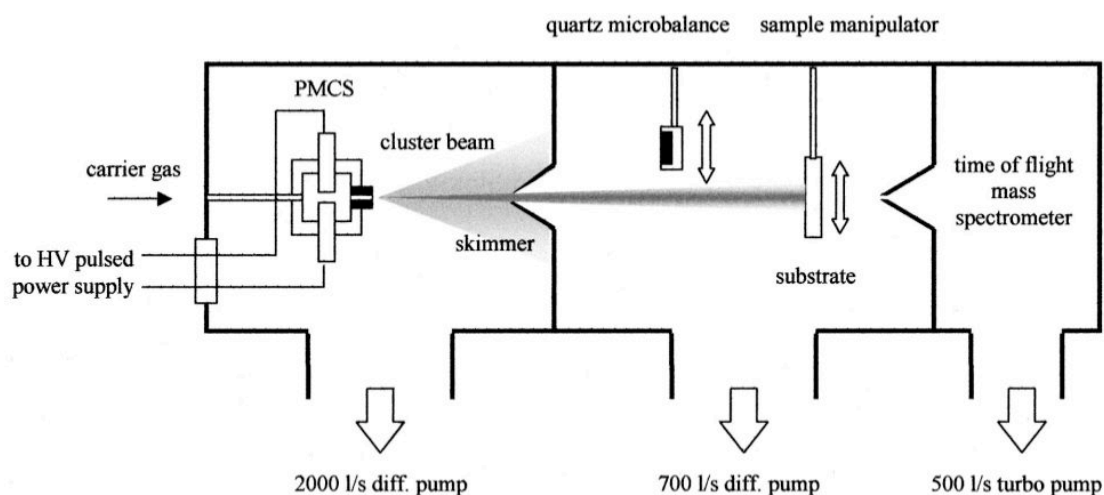


Fig. 2.6 Schematic representation of the supersonic beam apparatus for the deposition of cluster beams.

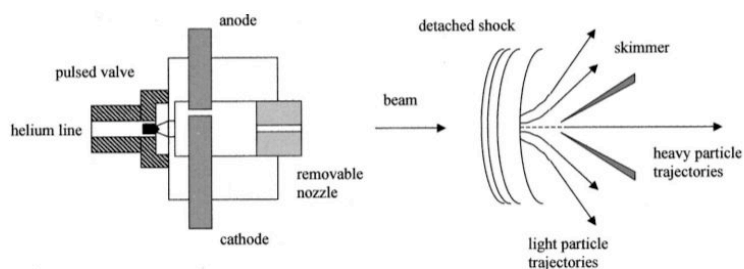


Fig. 2.7 Expanded view of the pulsed cluster source and of the region near the skimmer where a shock wave is formed. The trajectories of the heavy and light particles are schematically shown. Due to separation effects, films with different nanostructures can be deposited by placing a substrate to intercept different regions of the beam.

A supersonic beam is schematically described as a gas stream expanding very rapidly from a high pressure region (source), through a nozzle, to a low pressure region, Fig.2.6, Fig.2.7. The characteristics of the beam are mainly determined by the size and shape of the nozzle and by the pressure difference between the two regions. When a heavy species is diluted in a lighter one (as in the case of clusters diluted in He or another inert gas) and the mixture is expanded, there is the formation of a seeded supersonic beam. Figure 1 shows the principle of operation of the apparatus used for cluster beam deposition and based on a supersonic cluster source. It consists of three differentially evacuated chambers and it operates in the high vacuum regime. The first chamber hosts the cluster source and has a base pressure of typically  $1 \times 10^{-7}$  Torr, during source operation the average pressure is maintained in the range of  $1-3 \times 10^{-5}$  Torr. The supersonic cluster beam

enters the second chamber through an electroformed skimmer of 2 mm of diameter. The second chamber is equipped with a sample holder which can intersect the beam, a quartz microbalance for beam intensity monitoring; it can also host a beam-chopper or a fast ionization gauge for time of flight measurements of the velocity distribution of particles in the beam. During deposition the background pressure is typically  $1 \times 10^{-7}$  Torr. The third chamber hosts a linear time of flight mass spectrometer, which is placed collinear to the beam axis in order to achieve the best transmission. Carbon clusters have been produced by a pulsed microplasma cluster source (PMCS). The working principle of the PMCS is the following: A confined plasma discharge ablates a graphite rod in the cluster source. The vaporized carbon atoms are quenched by a pulse of helium and condense in clusters. The source consists of a ceramic body with a channel drilled to intersect perpendicularly a larger cylindrical cavity. The channel hosts two rods of the material to be vaporized. A solenoid pulsed valve facets one side of the cavity. The other side of the cavity is closed by a removable nozzle. The solenoid valve, backed with a pressure of 8 bar, delivers He pulses with an opening time of a few hundreds of microseconds. An intense helium jet is formed toward the cathode surface facing the valve. In this region the gas density is substantially higher than in the rest of the cavity. During standard operation the mean He pressure in the source cavity is of roughly 30 Torr. Just before the valve closing, a voltage ranging from 500 up to 1500 V is applied to the electrodes, causing the firing of the discharge and the production of the plasma localized in the region of the higher gas density. The ablation occurs when helium plasma strikes the cathode surface removing atoms via sputtering. The electrode surface where ablation occurs is very small and comparable to what is obtained in the case of laser vaporization, so that very precise paths can be burned on the cathode. The cathode is constantly rotated along its axis by a stepping motor external to vacuum to allow constant ablation conditions over 105 pulses. The mean pressure inside the first chamber is constantly monitored by a PC, connected to pressure gauge control units. To overcome the solenoid valve operation instabilities, a feedback chain automatically modifies the nominal opening time of the valve. This substantially increases the reproducibility of cluster synthesis conditions. With typical discharge conditions, we obtain a log-normal cluster mass distribution in the range of 0 – 1500 atoms/ clusters, with a maximum peaked at around 400 atoms/ cluster and an average size at about 950 atoms/cluster. The kinetic energy of the clusters is lower than 0.2 eV/atom, well below the binding energy of carbon atoms in the clusters. At cluster impact on the surface there is thus no substantial fragmentation of the aggregates and deposited films may keep memory of the structure the clusters had in the gas phase. The beam intensity has been tested in the second chamber selection it is thus possible to obtain very intense and collimated beams. Using a focusing nozzle we have obtained cluster beams with a divergence of 10 mrad and average densities of  $3 \times$

$10^{12}$  atoms/cm<sup>3</sup> ( $2 \times 10^{12}$  atoms/cm<sup>3</sup> pulsed) corresponding to rates of 2 nm/s at 300 mm distance from the source nozzle.

### **General Atomic carbon targets**

Other carbon targets were fabricated at General Atomics [37] (see Fig. 2.10) using a completely different technique based on the use of colloidal carbon. In this case, carbon with initial density  $\rho_0 = 1.6 \pm 0.10$  g/cm<sup>3</sup> was produced. Stepped targets were made through lathe machining of bulk aluminum. The Al base was  $\approx 8$   $\mu$ m, and the step thickness was  $\approx 8.5$   $\mu$ m. The carbon layer was then produced and the target was machined again to produce the C step (with thickness  $\approx 10$   $\mu$ m). The use of two different types of targets allow a comparison of measurements and better confidence in our results. Fig. 2.4 shows typical results obtained from the emissivity diagnostics for GA target while Fig. 2.6 is emissivity referred to sample in Fig. 2.5.

#### **2.1.4 Results**

In total, we obtained five good experimental points at LULI (two for  $\rho_0 = 1.45$  g/cm<sup>3</sup> and three for  $\rho_0 = 1.6$  g/cm<sup>3</sup>) and four good points at PALS (all for  $\rho_0 = 1.6$  g/cm<sup>3</sup>). These are shown in Fig. 2.12 with all the other experimental results already available in the literature in the pressure range  $P > 1.5$  Mbar. Data, grouped according to their initial density  $\rho_0$ , are compared to the shock polar curve derived from the Sesame tables (the model QEOS [38] yields practically identical results for carbon, even if it usually does not describe the Hugoniot with the same accuracy as the SESAME EOS does).

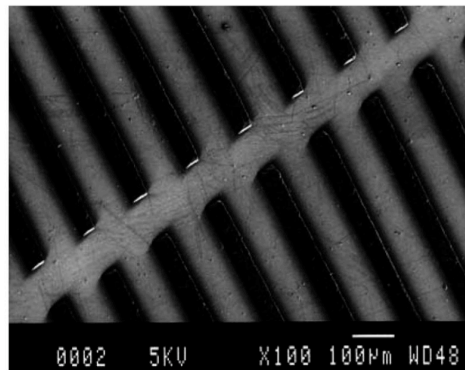


FIG. 2.8. SEM image of carbon steps with  $\rho_0=1.45$  g/cm<sup>3</sup> deposited on a CH/Al substrate. Al steps are not present since they were deposited later.

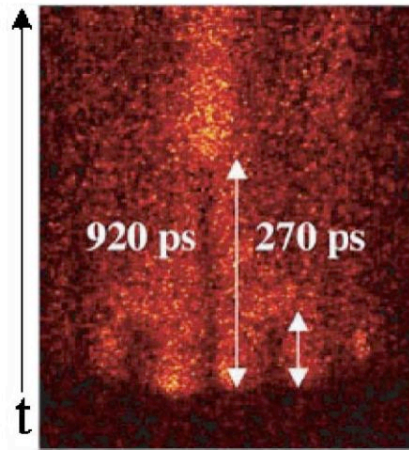


FIG. 2.9 Shock breakout streak image of the target rear side in emission. Shot energy was 25.3 J. Arrows indicate the shock breakout from the Al step (right) and from the C step (left). The size of the image is 600  $\mu\text{m}$  x 1.7 ns.

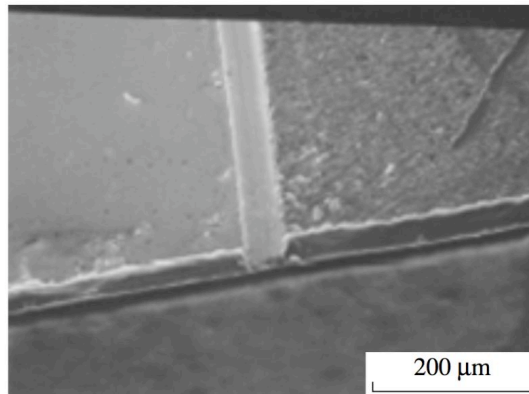


Fig. 2.10 SEM I image of double-step target produced at General Atomics, with density  $\rho_0 = 1.6 \text{ g/cm}^3$ .

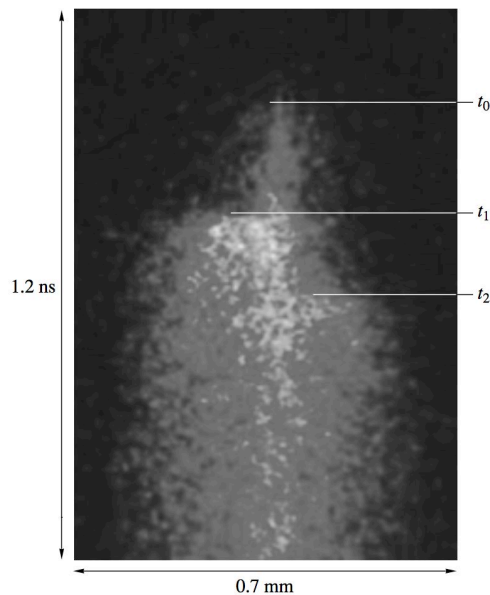


Fig. 2.11 Shock breakout streak image of the General Atomics target rear side in emission. Shot made at PALS with energy  $E = 108$  J. Lines indicate the shock break-out from the Al step (left) and from the C step (right). Al step gave  $t_1 - t_0 = 205$  ps,  $DA_1 = 38.8$  km/s,  $PA_1 = 33$  Mbar. C step gave  $t_2 - t_0 = 295$  ps,  $D_c = 32.2$  km/s,  $P_c = 18$  Mbar.

The errors in pressure and fluid velocity are  $\approx 15\%$  and  $\approx 20\%$ , respectively; these error bars were estimated by calculating the propagation of experimental errors on shock velocity (5%) on the quantities determined by the mismatch method. The error in shock velocity is instead determined from the experimentally measured uncertainties in step thickness and by the streak-camera temporal resolution. All our data, for both initial densities, are below the shock polar curve derived from the Sesame tables. Despite our quite large error bars (which make most points compatible with the theoretical curve), such results show a systematic deviation and indicate a compressibility of carbon at these pressures much higher than that predicted by most models (the density  $\rho$  of the compressed sample is obtained from the Hugoniot Rankine relations for shocks, namely from  $\rho(D-U) = \rho_0 D$ ). However, such behavior could be also due to the presence of systematic errors in our experiment. One possible cause often cited for explaining errors in laser-shock EOS experiments is preheating induced by X-rays. In our case, preheating was surely small for the points at LULI due to the rather low laser intensity and the presence of a CH layer on laser-irradiated side, which reduces X-ray generation (as shown experimentally in [35]). On the contrary, for the shots at PALS, preheating was measured by calibrating the emissivity diagnostics, and, for the two shots at higher energy (pressure), it was as high as a couple of eV [34].

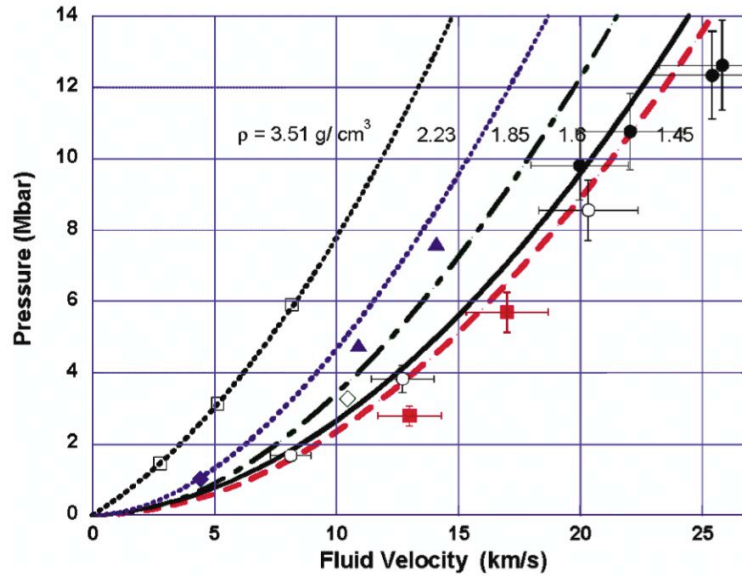


FIG. 2.12 Experimental EOS results from shock experiments. Only data with  $P > 1.5$  Mbar and corresponding Hugoniot are shown. Our points: full squares,  $1.45 \text{ g/cm}^3$ . LULI; empty circles,  $1.6 \text{ g/cm}^3$ . LULI; full circles,  $1.6 \text{ g/cm}^3$ . PALS. Previous points: empty diamond,  $1.85 \text{ g/cm}^3$ . Pavlovskii et al. [28]; triangles,  $2.2 \text{ g/cm}^3$ , Nellis [29]; full diamond,  $2.23 \text{ g/cm}^3$ , Pavlovskii et al. [28]; empty squares,  $3.51 \text{ g/cm}^3$  (diamond), Pavlovskii [30].

Despite this, the LULI points are as far from Sesame as the PALS points. Therefore, preheating is probably not the cause of deviation from theoretical curves (or at least not of the whole deviation). Another possible systematic effect could be due to the high porosity of the targets, even if porous and foam targets are routinely used in EOS experiments. Hence, even if this point requires further work and analysis, for the moment we can conclude that at very high pressures, carbon is likely to be more compressible than predicted by Sesame or QEOS. We should also note that a deviation from Sesame is also observed for other points obtained at high shock pressure (for instance, the point at  $\approx 3$  Mbar for carbon with  $\rho_0 = 1.85 \text{ g/cm}^3$  reported by Pavlovskii and Drakin [28]). Even more interestingly, the same behavior was observed by Nellis et al. [29], who, using underground nuclear explosions as a compression tool, report two EOS points for graphite ( $\rho_0 = 2.2 \text{ g/cm}^3$ ) at 4.76 and 7.61 Mbar. The relation between shock velocity  $D$  and fluid velocity  $U$  for carbon in the Megabar range is linear ( $D = C + SU$ , where  $C$  is the sound velocity in the material in that pressure range). For carbon with  $\rho_0 = 1.6 \text{ g/cm}^3$ , from Sesame (or QEOS), we get  $C \approx 5 \text{ km/s}$  and  $S \approx 1.27$  [39]. A linear interpolation of our points instead yields  $S \approx 1.08\text{--}1.14$  (depending on whether or not

we consider the two “preheated” points). From this, we get an “experimental” shock polar  $P = \rho_0 DU = \rho_0 (C + SU)$ , which of course nicely interpolates our results in the (P, U) plane. This curve is above the thermodynamic limit  $P = \rho_0 U^2$  corresponding to infinite compressibility (all our experimental points are above this limit). However, it seems too close to the shock polar for a perfect gas, which again could indicate the influence of systematic effects. For the case  $\rho_0 = 1.45 \text{ g/cm}^3$ , we did not make any attempt to determine S since we had only two points.

### **2.1.5 Conclusion**

The observed increased compressibility of carbon suggests that at a given pressure along the Hugoniot, the density in the final state (liquid) is smaller than that for solid. Transitions to less dense phases also enhance thermal contributions, explaining the observed pressure discrepancy. This agrees with conclusions by Nellis et al. [4] and reinforces their observations.

## **BIBLIOGRAPHY Part 1 Chapter 2**

1. J. A. van Vechten, Phys. Rev. B: Solid State **7**, 1479 (1973).
2. J. W. Shaner and J. M. Brown, **45**, 235 (1984).
3. R. Grover, J. Chem. Phys. **71**, 3284 (1979).
4. M. T. Yin and M. L. Cohen, Phys. Rev. Lett. **50**, 2006 (1983); M. T. Yin, Phys. Rev. B: Condens. Matter **30**, 1773 (1984).
5. R. Biswas, R. M. Martin, et al., Phys. Rev. B: Condens. Matter **30**, 3210 (1984).
6. S. Fahy and S. G. Louie. Phys. Rev. B: Condens. Matter **36**, 3373 (1987).
7. A. L. Ruoff and H. Luo, J. Appl. Phys. **70**, 2066 (1991).
8. H. K. Mao and P. M. Bell, Science (Washington, D.C.) **200**, 1145, (1978); H. K. Mao and R. J. Hemley, Nature (London) **351**, 721 (1991).
9. F. P. Bundy, Physica A (Amsterdam) **156**, 169 (1989); F. P. Bundy, J. Chem. Phys. **38**, 631 (1963); F. P. Bundy, H. M. Strong, and R. H. Wentorf, J. Chem. Phys. **10**, 213 (1973).
10. M. Grumbach and R. Martin, Phys. Rev. B: Condens. Matter **54**, 15730 (1996).
11. T. Sekine, Appl. Phys. Lett. **74**, 350 (1999).
12. L. Benedetti et al., Science (Washington, D.C.) **286**, 100 (1999).
13. S. Scandolo et al., Phys. Rev. B: Condens. Matter **53**, 5051 (1996).
14. A. Cavalleri et al., Europhys. Lett. **57**, 281 (2002).
15. In this regime, the most complete EOS are the SESAME tables Los Alamos Laboratory library: Report No. LALP-83-4, T4 Group LANL, Los Alamos, 1983).
16. M. Ross, Rep. Prog. Phys. **48**, 1 (1985).
17. S. Eliezer, A. Ghatak, and H. Hora *Equation of State: Theory and Applications* (Cambridge Univ. Press, Cambridge, U.K., 1986).
18. Y. Gupta and S. Sharma, Science (Washington, D.C.) **277**, 909 (1997).
19. S. Saumon, G. Chabrier, et al., Ap. J. Suppl. **99**, 713 (1995).

20. T. Guillot, Science (Washington, D.C.) **286**, 72 (1999).
21. M. Ross, Nature (London) **292**, 435 (1981).
22. F. Ancillotto, G. Chiarotti, et al., Science (Washington, D.C.) **275**, 1288 (1997).
23. W. J. Nellis, N. C. Holmes, et al., J. Chem. Phys. **107**, 9096 (1997); W. J. Nellis et al., Science (Washington, D.C.) **240**, 779 (1988).
24. N. F. Ness et al., Science (Washington, D.C.) **240**, 1473 (1989); N. F. Ness et al., Science (Washington, D.C.) **233**, 85 (1986).
25. J. E. Connerney et al., J. Geophys. Rev. **92**, 15329 (1987).
26. M. Koenig et al., Phys. Rev. E: Stat. Phys., Plasmas, Fluids, Relat. Interdiscip. Top. **50**, R3314 (1994).
27. M. Koenig et al., Phys. Rev. Lett. **74**, 2260 (1995);  
D. Batani et al., Phys. Rev. B: Condens. Matter **61**, 9287 (2000);  
D. Batani, A. Morelli, et al., Phys. Rev. Lett. **88**, 235502 (2002).
28. M. N. Pavlovskii and V. P. Drakin, JETP Lett. **4**, 116 (1966).
29. W. J. Nellis et al., J. Appl. Phys. **90**, 696 (2001).
30. M. N. Pavlovskii, Sov. Phys. Solid State **13**, 741 (1971).
31. W. H. Gust, Phys. Rev. B: Condens. Matter **22**, 4744 (1980).
32. *LASL Shock Hugoniot Data*, Ed. by S.P.Marsch (University of California, Berkeley, 1980), pp. 28–51.
33. K. Jungwirth et al., Phys. Plasmas **8**, 2495 (2001).
34. D. Batani, H. Stabile, et al., Phys. Rev. E: Stat. Phys., Plasmas, Fluids, Relat. Interdiscip. Top. (2003).
35. A. Benuzzi et al., Phys. Plasmas **5**, 2410 (1998).
36. E. Barborini et al., J. Phys. D: Appl. Phys. **32**, LI05 (1999);  
E. Barborini et al., Appl. Phys. Lett. **77**, 1059 (2000); P. Piseri et al.,  
Rev. Sci. Instrum. **72**, 2261 (2001).
37. Special thanks to J. Kaae, General Atomics, S. Diego, USA, for target fabrication.
38. R. M. More et al., Phys. Fluids **31**, 3059 (1988).
39. This is true for QEOS and the Sesame table 7830.  
Other carbon tables give different, but close, values.

# APPENDIX 1

## Working principle of Intense, Ultrashort laser

### A.1 Basic principle of generation of ultrashort pulses

The laser which provides the ultrashort pulse to be amplified is called the *oscillator*. An oscillator works on the principle of modelocking. A thorough description of modelocking and its history can be found elsewhere [212, 213].

The *modes* of oscillation of a laser are the self reproducing field distributions which are established in the optical cavity (figure A.1 up). A variety of such laser modes exist, with different field distributions normal to the resonator axis; these are termed *transverse modes*. Each of these transverse modes has an infinite set of eigenfrequencies or *longitudinal modes* (figure A.1 down) [12, 11]. In most mode-locked laser systems only the lowest order fundamental mode having a Gaussian profile is allowed to oscillate. The corresponding longitudinal modes have wavelengths,

$$\lambda_n = 2L/n, n \in N^+, \quad (\text{A.1})$$

where,  $L$  is cavity length. Thus a laser cavity supports an infinite number of possible longitudinal modes (the allowed frequencies in a cavity), but with completely unrelated phases. The first few modes in a laser cavity are illustrated in figure A.1. Among all the allowed modes, only those falling within the gain profile of the lasing medium would lase<sup>1</sup>. The profile is determined by the nature of the gain medium, the first and the most fundamental laser wavelength selector. With no mode selecting element placed in the cavity, the free-running laser modes oscillate independently, with random phases resulting

---

<sup>1</sup>The number of these modes,  $N = \Delta\nu_p/\nu_p = 2L/v_g$  (figure A.3), can vary from just a few (in HeNe lasers for example) to some  $10^4$  (in dye lasers and in Ti:sapphire lasers for example).

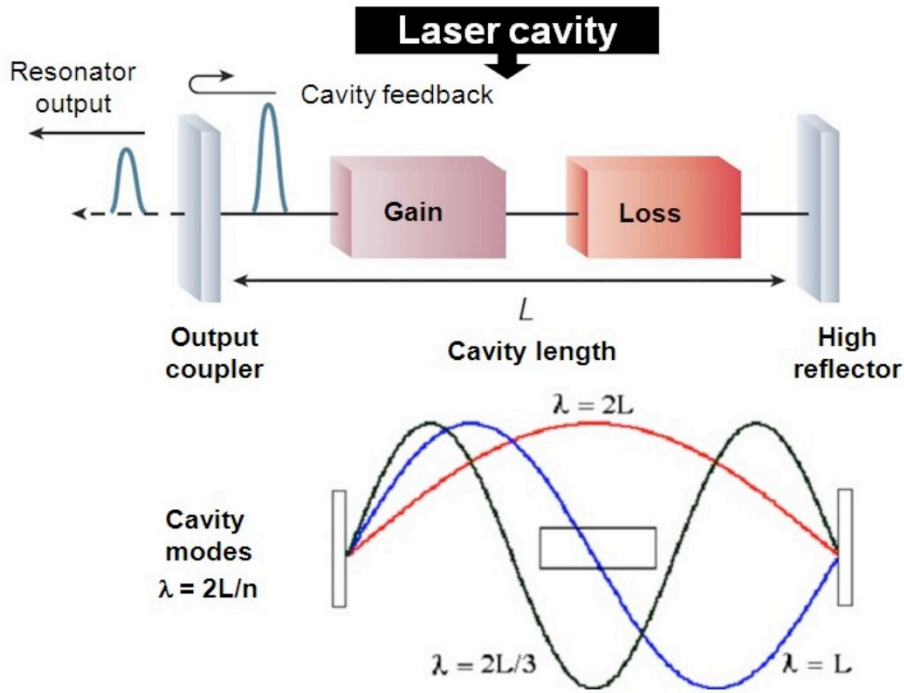


Figure A.1: The basic elements of a laser resonator (above) showing a gain medium, the feedback elements and cavity losses; and different possible longitudinal modes in a laser cavity (down), with mode spacing given by  $v_g/2L$ ,  $v_g$  is the group velocity.

in a laser output that is noisy and has no regular temporal structure.

To extract ultrashort pulses of well defined temporal structure one has to modelock the pulses. Modelocking, as the name suggests, involves locking a large number of longitudinal modes of a laser in phase. In a modelocked laser, the electric fields associated with the different modes interfere constructively at one point and destructively elsewhere to create a short spike of light. Mathematically, the Fourier transform of a large number of frequency components with same phase gives an infinite series of short pulses in time [214].

There are two ways a pulse can be modelocked: active and passive. In active modelocking, an externally (electronically driven) controlled optical loss modulator (typically using the acousto-optic or electro-optic effect) locks the modes. Passive modelocking, on the other hand uses an optically nonlinear medium ('saturable absorber' or 'Kerr lens and aperture combination') to create a self-amplitude modulation of the original light inside the laser cavity. Typically such nonlinear medium introduces loss to the intracavity laser radiation, which is relatively large for low intensities but significantly smaller for a short pulse with high intensity. The circulating pulse saturates the laser gain to a level

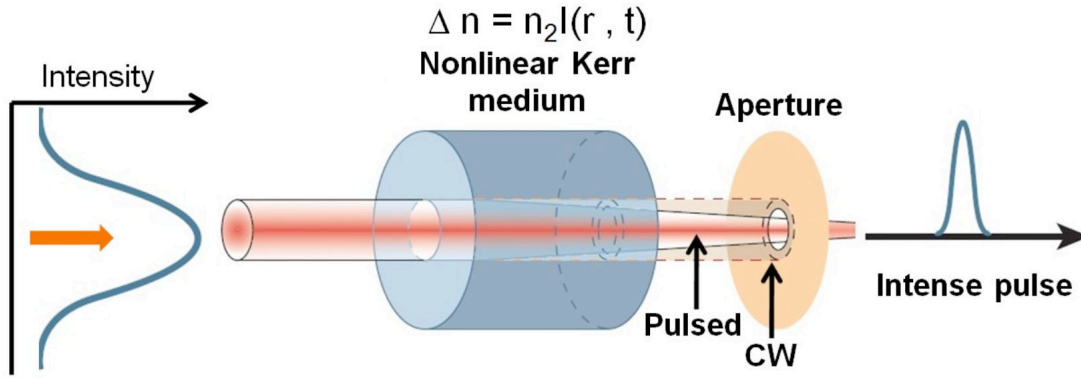


Figure A.2: A Kerr lens is generated when a high intensity pulse passes through a non-linear medium and induces a refractive index that depends on the transverse coordinates of the beam. Kerr lens modelocking (KLM) utilises formation of Kerr lens in a nonlinear optical media.

that is just sufficient to compensate for the losses from pulse itself, although any other circulating low-intensity light experiences more loss than gain and thus dies out during the following cavity round-trips. The underlying principle of modelocking is to strengthen the strongest of field fluctuations, at the expense of the weaker ones eventually leading to the concentration of the whole laser energy in a train of pulses. Details of modelocking can be found in [11, 14]. We will only discuss Kerr-lens mode-locking (KLM) [18] which is the backbone of the state-of-the-art table-top ultrashort Ti:Sapphire lasers, available today.

### A.1.1 Kerr-lens modelocking (KLM)

At high enough intensities, the refractive index (RI) of the medium then, is given by,  $n = n_0 + n_2 I$  [214, 215], where  $I$  is the intensity of the propagating field,  $n_0$  is the linear RI and  $\Delta n = n_2 I$  is the non-linear intensity-dependent refractive index. The phase delay experienced by a propagating optical signal is proportional to the refractive index (RI). An optical signal, thus, experiences a non-linear intensity-dependent phase delay due to  $n_2$  (in addition to the contribution from  $n_0$  to its phase) and this is known as *optical Kerr effect*. Kerr effect is a nonresonant non-linearity which, therefore, has no associated absorption and is a broadband phenomena (essentially wavelength independent). When the effect arises from the time dependence of intensity  $I$ , the phenomenon is called self phase modulation (SPM) and when it comes from the spatial variation of intensity it is called self focussing (shown in figure A.4). Optical Kerr effect leads to self-modelocking,

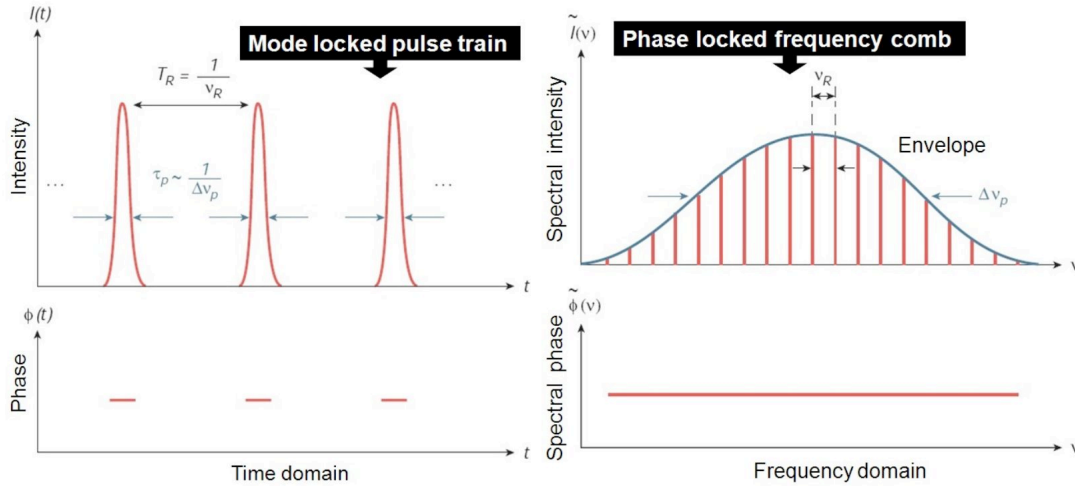


Figure A.3: Representation of modelocking in time domain (left) and frequency domain (right). The application of such pulses to ultrafast science (the time domain picture) and frequency standardisation techniques (the frequency domain picture) becomes clear from the two representations.

or self-locking [15] by self-phase modulation (SPM, discussed below) and self-focusing.

Kerr-lens modelocking is obtained through a Kerr lens at an intracavity focus in the gain medium or in another material, where the refractive index increases with intensity  $\Delta n = n_2 I(r, t)$ , where  $n_2 I$  is the nonlinear refractive index and  $I(r, t)$  the radial and time-dependent intensity of a short-pulsed laser beam. Hence as shown in figure A.2, in a laser cavity short bursts of light will then be focused in a Kerr medium differently compared to continuous waves (cw). To favor the pulsed mode over cw, the cavity is made unstable for cw-operation. In combination with a hard aperture inside the cavity (as shown in figure A.2), the cavity design is made such that the Kerr lens reduces the laser mode area for high intensities at the aperture and therefore forms an *effective fast saturable absorber*. Older designs used a hard aperture as shown in figure A.2, that simply cuts off the continuous part. In most modern designs, however, soft-aperture KLM is used, where the reduced mode area in the gain medium improves for a short time the overlap with the (strongly focused) pump beam and therefore the effective gain. As such effect is originated from the optical Kerr effect, the use of this technique for the mode-locking process is widely known as Kerr lens mode-locking (KLM). The obvious remaining question is how does passive modelocking like KLM start. Ideally, it starts from normal noise fluctuations in the laser. One noise spike is strong enough to significantly reduce its loss in the ‘effective saturable absorber’ and thus will be more strongly amplified during the following cavity round

trips, so that the stronger noise spike continues to further reduce its loss and continues its growth until reaching steady state, where a stable pulse train has been formed. In general, KLM lasers are not self-starting, that is, pulse formation does not start on its own, and additional perturbation to briefly increase laser noise is required. This is typically achieved by mechanically shaking one of the laser cavity mirrors.

Modelocked pulses are much shorter than the cavity round-trip time. An output coupler partially transmits a small fraction of the laser pulse out of the laser resonator equally spaced by the resonator round-trip time,  $T_R = 2L/v_g$  (figure A.1), where  $L$  is the laser cavity length and  $v_g$  the group velocity (that is, the propagation velocity of the peak of the pulse intensity). In the time domain, this means that a modelocked laser produces an equidistant pulse train, with a period defined by the round-trip time of a pulse inside the laser cavity  $T_R$  and a pulse duration  $t_p$  (figure A.3 left). In the frequency domain, this results in a phase-locked frequency comb with a constant mode spacing that is equal to the pulse repetition rate  $\nu_R = 1/T_R = v_g/2L$ , as illustrated in figure A.3. The spectral width  $\Delta\nu_p$  of the envelope of this frequency comb is inversely proportional to the pulse duration  $\tau_p$  (figure A.3).

### A.1.2 Self-phase modulation (SPM)

Self-phase modulation occurs in time domain. An ultrashort pulse of light, when travelling in a medium, will induce a varying refractive index of the medium due to the optical Kerr effect. This variation in refractive index will produce a time dependent phase shift in the pulse, leading to a change of the pulse's frequency spectrum. SPM takes place when the refractive index is modified on a time-scale comparable to or faster than the optical signal propagating through the medium. Then the pulse acquires a temporal phase profile.

A light pulse with intensity profile  $I(t)$ , propagating through a non-linear medium of length  $L$ , in addition to accumulating the usual linear phase  $\phi_0$ , will also experience an additional non-linear phase change which will be proportional to the intensity profile of the pulse giving a final phase,

$$\begin{aligned}\phi_f(t) &= \omega_0 t - \phi, \\ \phi &= (n + n_2 I(t)) L 2\pi / \lambda\end{aligned}\tag{A.2}$$

The first derivative  $d\phi_f/dt = \omega_f(t) = \omega_0 - (2\pi/\lambda)n_2 L dI(t)/dt$ , will correspond to a local change in frequency,  $-d\phi/dt = \delta\omega(t) = \omega_f - \omega_0 \propto -dI(t)/dt$ . Thus the non-linear intensity-dependent refractive index results in a frequency chirp (figure A.4). Since  $dI/dt$  is symmetric in time (for a Gaussian laser pulse), the extra frequencies generated through

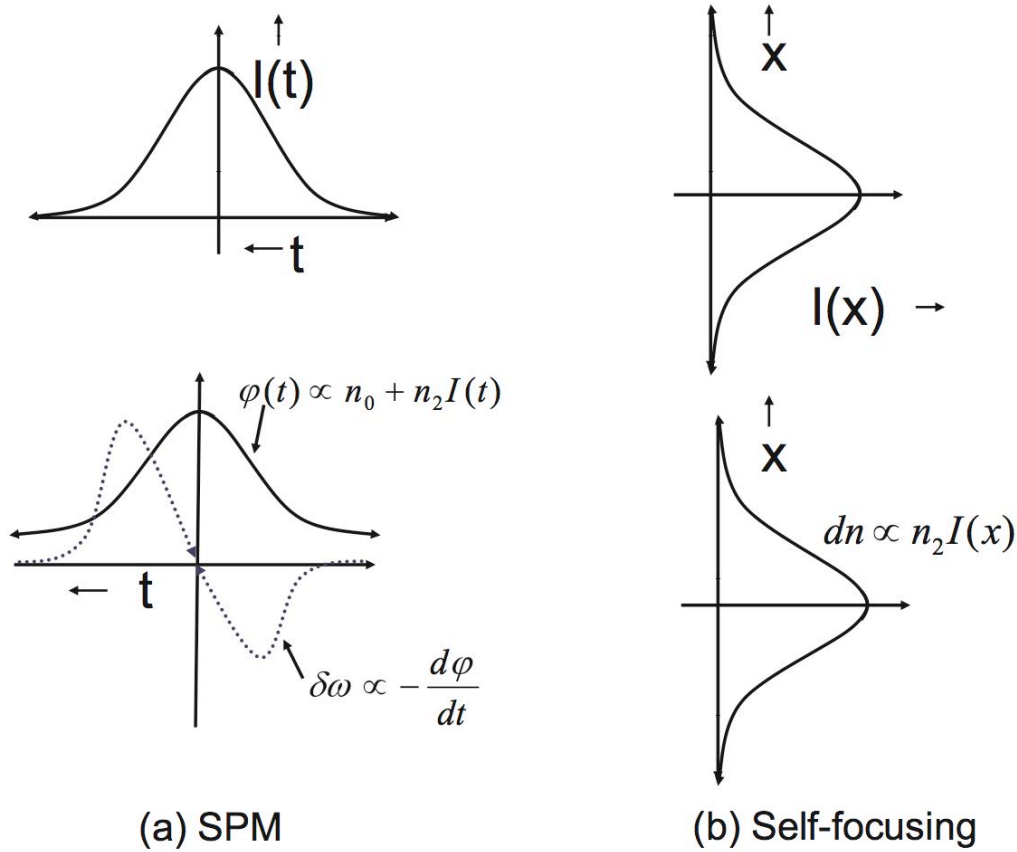


Figure A.4: Schematic of (a) SPM and (b) self-focusing. In the lower graph of (a), the intensity of  $\phi(t)$  and  $\delta\omega$  are not on the same scale.

SPM broaden the frequency spectrum of the pulse symmetrically. In the time domain, there is no change in the temporal profile (envelop) of the pulse due to only SPM [13]. However, in any real medium the effects of dispersion will simultaneously act on the pulse and the temporal profile of the pulse would get affected due to group velocity dispersion (GVD).

### A.1.3 Group velocity dispersion (GVD)

The different frequency components of an optical signal will propagate at different group velocities through a dispersive medium thereby causing group velocity dispersion (GVD). GVD changes the temporal profile of an optical signal without changing the spectral profile. The effect of propagation through a dispersive medium can, in principle, be reversed by propagation through a medium of the opposite dispersion. GVD arises from the dependence of group velocity ( $v_g = d\omega/dk$ ), on frequency, i.e. on  $\partial v_g/\partial\lambda$ . This is a property of the medium. GVD results in increase in pulse duration. The increased pulse

duration can be given as

$$t_{final} = t_0 \sqrt{1 + \frac{L}{L_D}} \quad (\text{A.3})$$

where  $L_D$  is the length over which the pulse width increases by  $\sqrt{2}$  [15].

The short pulses generated in the oscillator by the KLM are broadened due to GVD and need to be compressed to get the pulse of the order of few femtosecond temporal width.

#### A.1.4 Pulse compression using SPM and GVD

The instantaneous frequency chirp due to SPM,  $\delta\omega(t)$ , will be proportional to  $-dI(t)/dt$ . Thus for a gaussian pulse the front of the pulse where the medium experiences an increase of intensity with time,  $\delta\omega$  will be negative shifting the light towards lower frequencies. The peak of the pulse would have no frequency shift ( $dI(t)/dt = 0$ ). The medium will experience a decrease of intensity with time at the back of the pulse and so  $\delta\omega$  will be positive. Thus the frequencies would gradually be decreasing from the back to the front side of the pulse, i.e. with increasing time. Thus there would be positive chirp due to SPM for media exhibiting positive  $n_2$ . If this positively chirped signal then propagates in a medium which exhibits negative GVD (i.e. anomalous,  $d^2k/d\omega^2 < 0$  or  $\partial v_g/\partial\lambda < 0$ ) so that the group velocity increases for increasing frequency and higher frequencies travel faster, then the trailing edge of a chirped pulse containing the higher frequencies is

advanced while the leading half of the pulse containing the lower frequencies is retarded. The pulse then tends to collapse upon itself. This results in pulse compression.

Pulse compression thus arises when the non-linear frequency chirp and GVD have opposite signs (i.e. when  $n_2$  and  $d^2k/d\omega^2$  are of opposite sign). For the case when these quantities have the same sign, the back of the pulse will travel slower than the front and so dispersive pulse broadening would result.

#### A.1.5 A typical oscillator

We illustrate a typical source (oscillator) of ultrashort laser pulses by briefly describing Meera Seed oscillator, which is used for part of the experiments described in this thesis. The Ti:sapphire rod used in the cavity is cut at Brewster angle (5 mm or less in length), doped to absorb about 90% of the incident pump radiation and properly placed between two concave focusing mirrors (a high reflector and an output coupler). This crystal is pumped with a continuous wave (CW) green laser, usually a diode-pumped neodymium laser, (power of about 5W, in our case). The CW laser beam is allowed to propagate

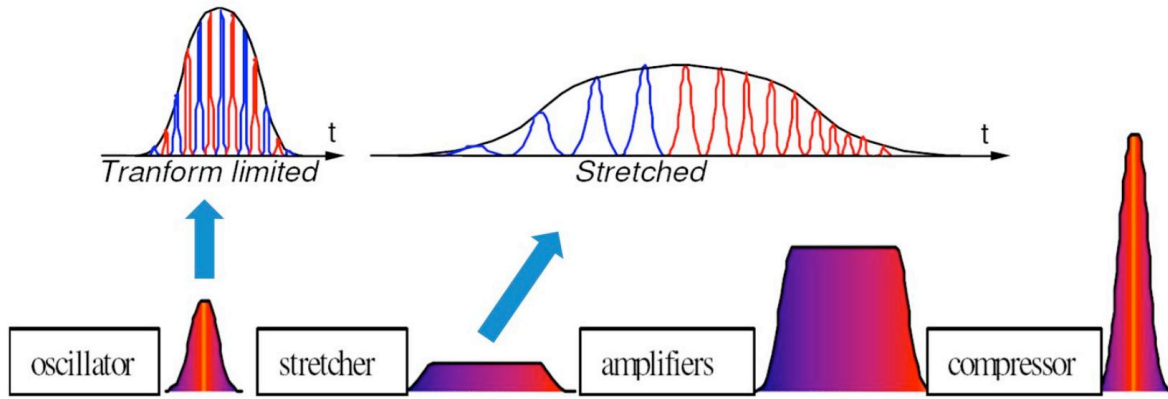


Figure A.5: The chirped pulse amplification

collinearly with the laser axis and focused (through the back of one of the mirrors which is transparent to green) into the Ti:sapphire rod. The optics inside the cavity is never dispersion-free (as discussed above), introduction of dispersion compensating elements in the cavity is a must. A pair of prisms is usually used for dispersion compensation, and recently CDMs (chirped dielectric mirrors) have also been used. Mode-locking is initiated by artificially perturbing the cavity which introduces a noise spike. This configuration delivers 90-fs pulses centered at 800 nm with 5-nJ energy/pulse at 76-MHz repetition rate

## A.2 Basic principle of amplification of ultrashort pulses (Chirped pulse amplification technique)

A normal femtosecond oscillator produces pulses of a few nJ of energy. To reach high peak intensities as mentioned in the introductory paragraph and also relevant to the thesis, the pulse energy should be amplified to the order of  $\sim 100$  mJs, i.e. a huge amplification factor of  $10^7 - 10^8$ . The main obstacles towards realising this goal earlier was twofold:

- Strong contribution of intensity dependent phase, which is undesirable in the amplifying stage.
- The bottleneck due to upper limits in intensity that an amplifying medium can withstand before optical damage.

Larger beam diameter in order to reduce the intensity, needed large-sized optical components in the amplifier- a prohibitively expensive way of realisation. Chirped-pulse amplification (CPA) [2] solved this problem. The CPA technique is the only available

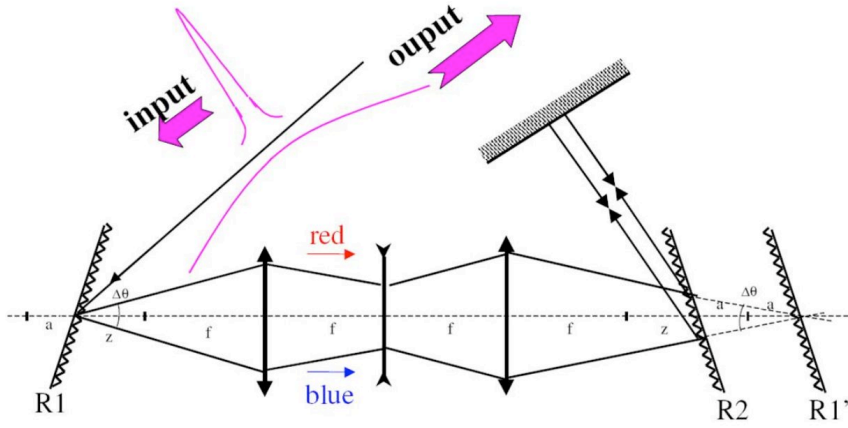


Figure A.6: Stretcher configuration. R1, R2 are gratings.

technique for amplifying short pulses ( $< 10$  ps) in solid-state materials. It consists in stretching the pulse by a factor  $10^3 - 10^5$  in order to reduce its peak power. Then the pulse is safely amplified in all stages of amplification. It is finally compressed back to a duration as close as possible to its initial value (see figure A.5).

### A.2.1 Pulse stretching

The most difficult part of CPA comes from the stretching and compression stages. In the first stage of CPA the ultrashort pulse is ‘stretched’ or elongated in time by introduction of ‘chirp’ (shifting frequencies in time as done by a chirping bird) in the pulse. The stretching has to be reversible (spectral filtering to lengthen the pulse is thus not allowed). The main known technique is based on the dispersion properties of gratings. Strickland and Mourou [2] first demonstrated the use of grating pairs for this purpose. The principle is to make each wavelength travel a different optical path. The ultrashort laser pulse is stretched out in time prior to introducing it to the gain medium using a pair of gratings. The gratings chirped, that is, the high-frequency component lags behind the low-frequency component, and has longer pulse duration than the original by a factor of  $10^3$  to  $10^5$ . Typically, the pulse duration is increased to 100 ps or more for efficient extraction of the stored energy.

### A.2.2 Amplification

Once the pulse is stretched so that its intensity is sufficiently below the damage limit of gigawatt per square centimeter, it is safely introduced to the gain medium and amplified by a factor of  $10^6$  or more. The large saturation fluence ( $1 J/cm^2$ ), long storage time ( $3\mu s$ ) and the huge bandwidth of Ti:sapphire make it an ideal amplifier gain material. Here we shall consider two basic schemes, the regenerative and the multipass amplifier. Usually in a big laser system there is one regenerative amplifier stage followed by multiple stages of multipass amplifiers depending on the requirement of pulse energy.

The regenerative amplifier (or regen) is a linear laser cavity which is seeded by the ps pulse output of the stretcher. The cavity geometry is designed usually to produce large gaussian beams from a relatively short cavity. It is pumped by a standard Q-switched Nd:YAG laser. The amplified mode is independent of the spatial distribution intensity of the seeded beam. The gain of this amplifier is around  $10^5$ . Once pumped and even without seeding, this resonator acts as a Q-Switch cavity by way of polarization switching in a Pockels cell. In regenerative amplification, a single vertically-polarized pulse from the stretcher, called the ‘seed’, is injected into the amplifier using a fast-switching Pockels cell. This is performed by stepping the voltage in two stages, firstly by a quarter wave, in order to trap the pulse in the amplifier cavity and then up to a half wave for ejection. Typically, the pulse makes around 12-13 round trips in the cavity before the gain is saturated. A Faraday rotator is used to isolate the output pulse from the input.

The next stage of the amplification of femtosecond pulses is based on the multi-pass scheme. This section does not form a cavity. The amplified pulse from the regenerative amplifier is injected into the multipass amplifier, where it is allowed to make typically 4-6 passes before being ejected into the compression stage.

### A.2.3 Pulse compression

An optical compressor is based on a process opposite of stretching. The laser pulse at the output of the final amplifier is re-compressed back to the original pulse width in this stage. Here gratings are set in a *subtractive diffraction geometry*, where red components of the light pulse have a longer optical path than blue ones as shown in figure A.7. Thus the various components of a positively dispersed pulse can be reset in phase. Depending on

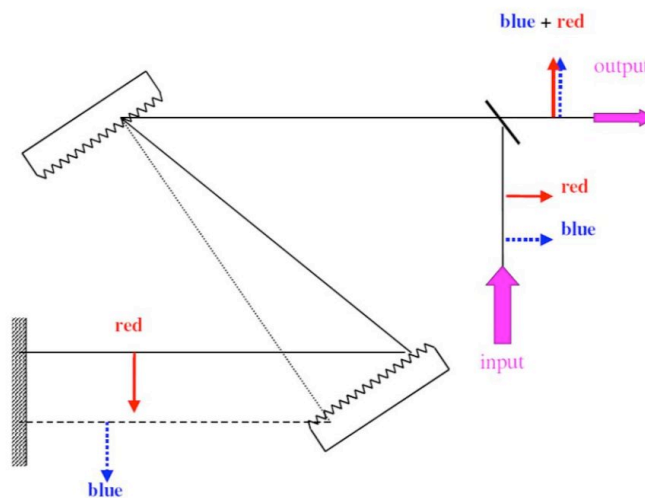


Figure A.7: Compressor configuration.

the energy level of the compressed pulse the whole compressor and the beam afterwards is usually kept inside high vacuum to protect the beam from distortion due to nonlinearities and the optics from damage.